



UNIVERSITÀ DELLA CALABRIA



UNIVERSITA' DELLA CALABRIA
Dipartimento di Ingegneria Meccanica, Energetica e Gestionale

***Dottorato di Ricerca in
Ingegneria Meccanica***

Con il contributo di

Commissione Europea, Fondo Sociale Europeo e Regione Calabria

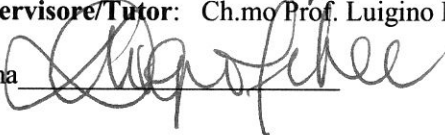
CICLO XXVI

TITOLO TESI

**ADVANCED NUMERICAL METHODS
FOR MATERIAL FORMING AND CUTTING**

Settore Scientifico Disciplinare ING/IND-16

Coordinatore: Ch.mo Prof. Leonardo Pagnotta
Firma 

Supervisore/Tutor: Ch.mo Prof. Luigino Filice
Firma 

Dottorando: Dott. Francesco Greco

Firma 

Abstract

The finite element method is the reference technique in the simulation of metal forming and provides excellent results with both Eulerian and Lagrangian implementations. The latter approach is more natural and direct but the large deformations involved in such processes require remeshing-rezoning algorithms that increase the computational times and affect the quality of the results. For this reasons alternative techniques based on modified FEM formulations or meshless approximants are worth to be investigated. In particular, in this project, the finite element method with nodal integration and the *maximum entropy* meshfree approximants are studied and applied to the simulation of selected problems in metal forming and orthogonal cutting.

Il metodo degli elementi finiti è attualmente la tecnica di riferimento nella simulazione di processi di formatura e fornisce ottimi risultati sia con formulazioni Euleriane che Lagrangiane. Quest'ultimo approccio è più naturale e diretto ma le grosse deformazioni che entrano in gioco in questi processi richiedono l'applicazione di algoritmi di remeshing-rezoning che aumentano i tempi computazionali e peggiorano la qualità dei risultati. Per questi motivi assume particolare interesse lo sviluppo di tecniche alternative, basate su formulazioni FEM modificate o su approssimazioni senza maglia (meshless). In particolare, in questo lavoro, sono studiati il metodo degli elementi finiti con integrazione nodale e le tecniche meshless di tipo *maximum entropy* e, inoltre, sono applicati alla simulazione di processi di formatura e taglio.

Contents

List of Figures	v
1 Introduction	1
2 The Nodal Integrated Finite Element Method	4
2.1 Introduction	4
2.2 The nodal integration formulation	6
2.2.1 Stabilization	10
2.3 A comparison between the different NI schemes and their stabilization in the simulation of extrusion	10
2.4 Simulation of orthogonal cutting	18
3 The <i>maximum entropy</i> approximants	22
3.1 Introduction	22
3.2 The <i>maximum entropy</i> approximants	25
3.3 Derivatives of max-ent basis functions on the boundary of the domain	29
4 Blending between isogeometric and max-ent approximants	32
4.1 Introduction	32
4.2 The IGA-LME formulation	33
4.3 Numerical Integration	34
4.4 Simulation of contact problems	39
4.4.1 Formulation	40
4.4.2 Hertz's cylinders problem	41

4.4.3	Contact of a semi-circular indenter	44
4.4.4	Contact of a complex-shaped indenter	45
5	Simulation of forming processes with max-ent approximants	48
5.1	Introduction	48
5.2	The stabilized viscoplastic formulation	50
5.3	Numerical examples	55
5.3.1	Upsetting	55
5.3.2	Extrusion	57
5.3.3	Orthogonal cutting	60
6	Concluding remarks	62
	References	64

List of Figures

2.1	An example of Voronoi diagram	6
2.2	The GV integration scheme	8
2.3	Simulation of a plain strain extrusion process	11
2.4	The meshes used for the simulation	13
2.5	The effects of the regularity of the mesh	14
2.6	The effects of the stabilization	15
2.7	The flow stress at the end of the simulation	16
2.8	Effects of the stabilization on the stress field	17
2.9	Simulation of orthogonal cutting	18
2.10	The dynamical mesh generation	19
2.11	The cutting force	20
2.12	The pressure on the rake face	21
2.13	The predicted geometry	21
3.1	Seamless transition from meshfree to Delaunay affine basis functions	28
3.2	Basis functions, gradient and Hessians (one-dimensional LME). . .	30
3.3	Plot of LME properties.	31
4.1	IGA-LME blending for a circular domain	35
4.2	Numerical integration	37
4.3	The linear elasticity patch test	38
4.4	The master and the slave surfaces and the gap function.	40
4.5	Simulation of the Hertz's problem	43
4.6	Contact of semicircular indenter	44
4.7	Contact of a complex-shaped indenter	46

LIST OF FIGURES

5.1	Upsetting	56
5.2	Extrusion	58
5.3	Comparison between NI-FEM and LME pressure fields	59
5.4	Pressure along the symmetry axis and on the bottom of the die .	59
5.5	Orthogonal cutting	61

1

Introduction

The finite element method (FEM) has been successfully applied to the simulation of all the types of metal forming process (1, 2) and, thanks to the increasing computer power, it can provide excellent results with reasonable computational times. Thanks to its flexibility and robustness commercial FEM codes are a standard tool in the industry. However, the main limitation of the FEM in this kind of applications is that the quality of the results displays mesh dependency (3). When a Lagrangian formulation is used the mesh moves with the material and, if the element become too distorted, the numerical results loose their accuracy. In this case nodal adaptation procedures, that in the FEM framework are known as remeshing techniques, are required to proceed with the analysis. As drawback, these techniques increase the computational cost and introduce additional errors when the variables are mapped from the old mesh to the new one. In addition the flexibility of the method is reduced especially in three dimensions where, although some commercial codes show a good performance with tetrahedral meshes and extensive remeshing, good mesh generation algorithms are still a topic of investigation (4).

Eulerian formulations have been also employed in several metal forming (5, 6, 7) and cutting (8) applications but other drawbacks such as determining the geometry of the free surface of the flow are present with this approach. Also the arbitrary Lagrangian-Eulerian formulation (ALE) has been shown to perform

well both for metal forming (9, 10, 11) and cutting (12, 13) but it presents some limitations such as controlling the mesh motion.

For these reasons, even if the classical FEM provides very good results in many applications, researchers are currently focusing their attentions also on innovative techniques based on modified FEM formulations or on meshless approximation schemes (14). Within the former framework nodal integration (NI) has been recently proposed as a technique which improves the performance of standard tetrahedral elements and avoids volumetric locking in the study of incompressible materials (15). On noting that the NI formulation is not affected by mesh distortions the method appears extremely suitable for the simulation of material forming processes. This motivated the investigation on the NI schemes and on their application to this field. In particular, in this work, different NI formulations are analysed and applied to benchmark metal forming and orthogonal cutting processes. The results found in such investigation are satisfactory for many aspects and constitute an encouraging starting point to further develop the method. However, some issues associated to improper oscillations in the numerical solutions of the problems provided an additional motivation to investigate also on the application of meshless methods.

These methods, also known as meshfree techniques, have been used in the last years for treating a large variety of problems, especially where large deformations are involved, such as in the forming processes. In contrast to finite elements, meshless methods require only nodal data to construct the approximants (which are usually called basis functions in opposition to the FEM shape functions) and no explicit connectivity between nodes has to be defined. The approximation accuracy is not significantly affected by the nodal topology and therefore, in problems involving large deformations, the natural evolution of the initial nodal discretization can be used in Lagrangian implementations. In addition the eventual introduction, elimination or repositioning of nodes become a trivial task, since no geometrical restriction on the characteristics of the mesh exists.

Within the family of meshfree approximation schemes the *local maximum entropy* approximants have been recently proposed and have been shown to possess interesting advantages respect to other meshless approximants (16). For this reason, in this work, their application is extended also to metal forming and cutting

problems. Furthermore original contributions to the numerical development of *maximum entropy* methods are introduced.

The outline of the thesis is the following: in chapter 2 the application of nodal integration to the FEM is discussed and the relative numerical results are presented. In Chapter 3 after a brief review on meshless methods the formulation of the *maximum entropy* approximants is introduced. In chapter 4 some original contributions to the blending between *maximum entropy* and isogeometric approximants (17) are exposed. Then in chapter 5 a formulation to apply the *maximum entropy* approximants to viscoplastic flows is presented. Also in this case some numerical results in the simulation of benchmark metal forming and orthogonal cutting processes are shown. Finally in chapter 6 some concluding remarks are given and possible future developments are analysed.

2

The Nodal Integrated Finite Element Method

2.1 Introduction

The nodal integration (NI) is a technique that has been introduced in both FE and meshless methods. In the first case it has been proposed as an alternative to the standard integration that requires the generation of a mesh in opposition to the meshfree character that this family of methods should supply. Furthermore with nodal integration the computation of the derivatives of the basis functions can be avoided in a standard Galerkin implementation, which simplifies the numerical implementation for those approximants whose derivatives are difficult to calculate.

In the FEM case the integration is straightforward to realize. However, the nodal integration showed some interesting properties that encouraged the researchers to apply this technique also to finite elements. As it is well known, in the FEM environment, the performances of the analysis depend on the type of element. The constant strain elements (triangle with 3 nodes or tetrahedrons with 4 nodes in the 3D case) would be preferable for different reasons, especially when non-linear problems are investigated. Nevertheless their poor performances in acute bending problems and incompressible materials simulation force researchers

to use high-order elements, such as 8 nodes tetrahedral or hexahedral elements. Anyway these formulations are not free from the results worsening due to the mesh deterioration and, besides, the remeshing procedure is very costly to be implemented, particularly for the hexahedral elements.

A great drawback of traditional FEM methods is that the numerical model is always stiffer than the studied material. What is more, any mesh distortion gives a further spurious stiffness to the model. Introducing a Nodal Integration scheme the FEM model is generally less stiff and, therefore, a distorted mesh could paradoxically have a beneficial effect on the performances. The remeshing step can then be avoided in many applications or anyway consistently reduced.

Another advantage that is introduced with the nodal integration is that the volumetric locking problems in the study of incompressible materials (this is the case of metal forming), that are typical of standard finite elements, are avoided with the new formulation. Thanks to this property mixed formulations are no longer necessary to deal with incompressibility and the performance is significantly improved.

The basics of nodal integration in FE analysis were firstly introduced in (15) where they showed that applying the new technique the performances of the constant strain elements are significantly improved in the study of acute bending problems. Moreover the method was shown to be free from volumetric locking in the simulation of quasi-incompressible materials. In (18) they noted that the formulation proposed in (15) was prone to spurious low energy oscillations and introduced a new stabilized nodal integrated tetrahedral element. They also analytically showed that their new element was stable and consistent for linear elasticity.

In the meshless environment the nodal integration was firstly introduced in (19) and then modified in (20, 21) to avoid spurious zero energy oscillations. This approach is based on an averaging of the strain that is analogous to the method employed in (15) for the finite elements and, in fact, low energy oscillations are still present. In (22) the stabilization approach presented in (18) for the FEM is extended also to meshless methods.

In this chapter the numerical formulation of nodal integration is reviewed in section 2.2 and the different NI schemes are presented. Then their performance

and the effect of the stabilization are studied in the simulation of an extrusion process in section 2.3, while in section 2.4 the method is applied to the simulation of an orthogonal cutting process.

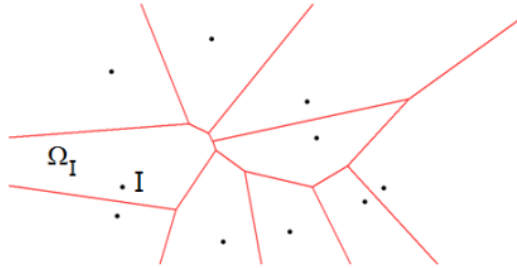


Figure 2.1: An example of Voronoi diagram.

2.2 The nodal integration formulation

Let Ω be a 2D computational domain discretized by a cloud of nodes, enumerated from 1 to N_N and denoted by I , and a mesh of triangular elements, enumerated from 1 to N_E and denoted by J . In a traditional finite element code, the strain is calculated using the gradient matrix \mathbf{B} , that, if $\varphi_1, \varphi_2 \dots \varphi_{N_N}$ are the shape functions, is defined as:

$$\mathbf{B} = \begin{pmatrix} \varphi_{1,x} & 0 & \dots & 0 \\ 0 & \varphi_{1,y} & \dots & \varphi_{N_N,y} \\ \varphi_{1,y} & \varphi_{1,x} & \dots & \varphi_{N_N,x} \end{pmatrix} \quad (2.1)$$

Thus, if \mathbf{d} is the vector containing the (unknown) nodal displacements, the strain is given by:

$$\boldsymbol{\varepsilon}(\mathbf{x}) = \mathbf{B}(\mathbf{x})\mathbf{d} \quad (2.2)$$

If three-node triangular elements are used, the shape functions derivatives are constant in every element, and also the matrix \mathbf{B} . Thus the elements strain can be expressed as:

$$\boldsymbol{\varepsilon}_J = \mathbf{B}_J\mathbf{d} \quad (2.3)$$

2.2 The nodal integration formulation

and, if \mathbf{E} is the constitutive matrix, the stiffness matrix \mathbf{K} is assembled in the following way:

$$\mathbf{K} = \int_{\Omega} \mathbf{B}^T \mathbf{E} \mathbf{B} d\Omega = \sum_{J=1}^{N_E} \mathbf{B}_J^T \mathbf{E} \mathbf{B}_J A_J \quad (2.4)$$

where A_J is the area of each element.

When the nodal integration is applied to FEM a constant strain field $\tilde{\boldsymbol{\varepsilon}}_I$ is assumed within a particular volume \tilde{V}_I , associated to each node. The easiest to interpret NI scheme is the one proposed in (20), that is based on the Voronoi diagram (23). According to figure 2.1 the Voronoi diagram is a subdivision of the computational domain in regions Ω_I , where each region is associated with a node I , so that any point in Ω_I is closer to the node I than to any other node in the domain. In this case the nodal volume \tilde{V}_I is, for each node, the area A_I of the corresponding cell in the diagram and the assumed strain is the average strain in this cell:

$$\tilde{\boldsymbol{\varepsilon}}_I = \frac{1}{A_I} \int_{\Omega_I} \boldsymbol{\varepsilon}(\mathbf{x}) d\Omega \quad (2.5)$$

Since constant strain elements are used, equation 2.5 could be rewritten as:

$$\tilde{\boldsymbol{\varepsilon}}_I = \frac{1}{A_I} \sum_{J=1}^{N_E} \boldsymbol{\varepsilon}_J \text{Area}(\Omega_I \cap T_J) \quad (2.6)$$

where T_J are the triangular elements in which the strain remains constant (figure 2.2). Observing that $\sum_{J=1}^{N_E} \text{Area}(\Omega_I \cap T_J) = A_I$ we can note that the strain $\tilde{\boldsymbol{\varepsilon}}_I$ is a weighted average of the strain of the elements. From now on we will refer to this scheme as Global Voronoi Integration (GV).

In (15) two NI schemes are proposed. They also provide a strain averaging, but the weights are different. In particular it is imposed that the strain $\tilde{\boldsymbol{\varepsilon}}_I$ depends only on the strain of the set of elements S_I that contain the node I . According to this constraint, one of the two schemes is also based on the Voronoi Diagram, but in this case the Diagram is locally calculated the triangles. In particular each triangle T_J is divided in three zones t_{JI} , associated to its nodes, so that every point in $\tilde{\boldsymbol{\varepsilon}}_I$ is closer to the node I than to any other node in T_J . Then the nodal

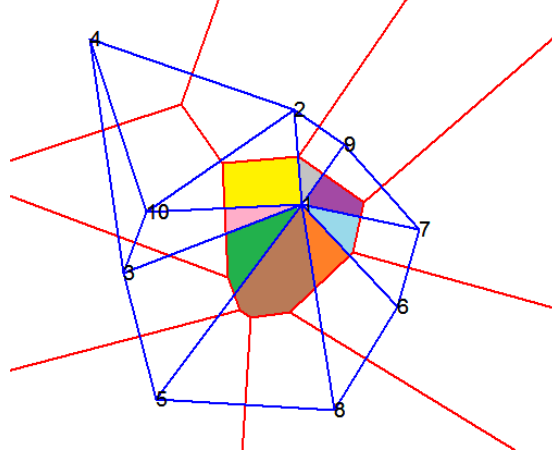


Figure 2.2: The GV integration scheme - The assumed strain is a weighted average of the elements strain. In the numerical implementation all the coloured areas have to be calculated.

volume and the assumed strain are calculated as:

$$\tilde{V}_I = \sum_{J \in S_I} Area(t_{JI}) \quad (2.7)$$

$$\tilde{\boldsymbol{\varepsilon}}_I = \frac{1}{\tilde{V}_I} \sum_{J \in S_I} \boldsymbol{\varepsilon}_J Area(t_{JI}) \quad (2.8)$$

We will refer to this scheme as Local Voronoi Integration (LV). The other technique proposed in (15) is not based on geometrical considerations but provides a heuristic calculation of the assumed strain, imposing that the area of the triangles is divided in three equal parts, associated to its nodes. Hence:

$$\tilde{V}_I = \sum_{J \in S_I} \frac{Area(T_J)}{3} \quad (2.9)$$

$$\tilde{\boldsymbol{\varepsilon}}_I = \frac{1}{\tilde{V}_I} \sum_{J \in S_I} \boldsymbol{\varepsilon}_J \frac{Area(T_J)}{3} \quad (2.10)$$

This scheme will be called Direct Averaging Integration (DA).

Similarly to a traditional FE interpolation the assumed strain could be related to the displacement field using an equivalent gradient matrix:

$$\tilde{\boldsymbol{\varepsilon}}_I = \tilde{\mathbf{B}}_I \mathbf{d} \quad (2.11)$$

2.2 The nodal integration formulation

It is easy to demonstrate that the matrices $\tilde{\mathbf{B}}_I$ will be a weighted average of the elements matrices \mathbf{B}_J , calculated using the same weight coefficients of the strain case, depending on the specific NI scheme. Thus, in the implementation of the method, the matrices $\tilde{\mathbf{B}}_I$ are calculated and the global stiffness matrix is assembled as:

$$\tilde{\mathbf{K}} = \sum_{I=1}^{N_N} \tilde{\mathbf{B}}_I^T \mathbf{E} \tilde{\mathbf{B}}_I \tilde{V}_I \quad (2.12)$$

This last calculation takes an additional computational time that is negligible respect to a traditional FEM code when DA scheme is used. In fact, only the volume of the elements has to be calculated and the equivalent gradient matrixes are directly calculated as a linear combination of the element gradient matrixes. The situation changes in the Voronoi-based (GV and LV) techniques. In particular in the GV case all the areas of the intersections between a given Voronoi cell and the elements have to be calculated (see figure 2.2). In this work this operation has been carried out describing both the cells and the elements as convex polygons and then applying the Lasserre algorithm (24). Although the computational complexity is linear with the number of nodes this is a significant time consuming operation that could take a computational time of the same order or slightly higher than the total time consumed for the analysis by a traditional FEM code. Anyway, the asymptotical linear complexity ensures that for clouds composed by a high enough number of nodes this time tends to be smaller than the time requested for the resolution of the equations. The LV scheme could be also implemented describing the geometrical entities by convex inequalities and applying the Lasserre algorithm or other similar. Nevertheless in order to advantage the rapidity of the simulation other more efficient strategies are possible. In particular, after determining the coordinates of the circumcenters of the triangular elements, the intersections areas could be find out calculating the areas of particular triangles. This operation takes a practically negligible time, as in the DA case.

2.3 A comparison between the different NI schemes and their stabilization in the simulation of extrusion

2.2.1 Stabilization

According to (18), in order to avoid the low energy spurious mode typical of standard Nodal Integration, a stabilized stiffness matrix \mathbf{K}_S is assembled using a stabilization parameter α and the modified behaviour matrix $\tilde{\mathbf{E}}$. In particular for linear problems we have:

$$\mathbf{K}_S = \mathbf{K}_{NOD} + \mathbf{K}_{ELEM} = \sum_{I=1}^{N_N} \tilde{\mathbf{B}}_I^T (\mathbf{E} - \alpha \tilde{\mathbf{E}}) \tilde{\mathbf{B}}_I \tilde{V}_I + \alpha \sum_{J=1}^{N_E} \mathbf{B}_J^T \tilde{\mathbf{E}} \mathbf{B}_J A_J \quad (2.13)$$

The influence of α on the results will be discussed in section 2.3; the matrix $\tilde{\mathbf{E}}$ differs from \mathbf{E} because when incompressible materials are studied it is assembled using a different Poissons coefficient ν , since locking problems would be present in the elementary matrix \mathbf{K}_{ELEM} . A value of $\nu \sim 0.4$ is generally employed.

2.3 A comparison between the different NI schemes and their stabilization in the simulation of extrusion

Extrusion is a typical example of forming process in which the large deformations stress the classical FE formulation. Therefore the performances of the three NI schemes have been compared in the simulation of the plain stress extrusion process illustrated in figure 2.3.

As far as the material behaviour is considered, in the forming processes and in particular in extrusion, strains are very large as compared to elastic ones. Thus the most extended approach employed in the last decades in the FEM environment is the so called *flow formulation*(25), that was firstly proposed by Zienkiewicz (5, 6). Even if an elastic recover exists at the die outlet it is an accepted assumption to neglect it and therefore to relate the Cauchy stress only to the strain rate tensor. This gives a viscoplastic formulation that resembles that of non-newtonian fluids, which inspired the term *flow formulation*. The great advantage of this approach is that velocities can be directly assumed as essential

2.3 A comparison between the different NI schemes and their stabilization in the simulation of extrusion

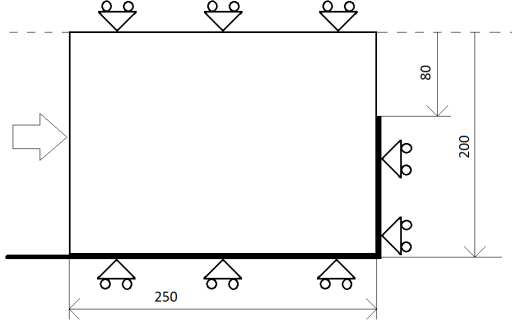


Figure 2.3: Simulation of a plain strain extrusion process - Sketch of the model.

variables of the problem instead of displacements. Within the viscoplastic formulation several models can be adopted to describe the material behaviour. Among these the so called Sellarg-Tegart law (26) has been used in many references applications (27, 28). Anyway, since the scope of this work was only to investigate on the potentialities of the new techniques a simpler Northon-Hoff model (29) was preferred. Other simplifications were made, such as neglecting friction and thermal phenomena. The Northon-Hoff model takes the form of a power law:

$$S_f = C\bar{\dot{\epsilon}}^n \quad (2.14)$$

where S_f is the flow stress and $\bar{\dot{\epsilon}}$ is the equivalent strain rate. The coefficients employed in this study were C and $n = 0.2$ that, according to (30), are typical of some aluminium alloys.

When nodal integration is introduced the model is free of volumetric locking and, therefore, it is not necessary to employ mixed formulation to deal with incompressibility. The stress is related directly to the strain rate, analogously to an elastic problem:

$$\boldsymbol{\sigma} = \mathbf{E}\dot{\boldsymbol{\epsilon}} \quad (2.15)$$

where, in the case of plain strain:

$$\mathbf{E} = \mu \frac{2\nu}{1-2\nu} \begin{bmatrix} 1-\nu & \nu & 0 \\ \nu & 1-\nu & 0 \\ 0 & 0 & \frac{1-2\nu}{2} \end{bmatrix}. \quad (2.16)$$

2.3 A comparison between the different NI schemes and their stabilization in the simulation of extrusion

In order to impose incompressibility a value of $\nu \rightarrow 0.5$ is adopted. In fact, the choice $\nu = 0.5$ is not possible since a singular constitutive matrix would be obtained. In the practice the problem is solved by introducing a numerical penalization that consists in assuming a value of ν very close to 0.5. In this application the value of $\nu = 0.499999$ was used. The viscosity μ also depends on the strain rate and gives non-linearity to the problem:

$$\mu = \mu_0 \bar{\epsilon}^{n-1} = \frac{C}{3} \bar{\epsilon}^{n-1}. \quad (2.17)$$

An iterative approach is required for the resolution of the constitutive equations. The Newton Raphson would be the best choice because of his rapidity but when highly non-linear problems are studied it does not converge unless an initial solution close enough to the final one is used. On the contrary the Direct Iteration Method (1) requires some more iterations but it is more robust and less sensible to the values of the initial solution, even in highly non-linear problems. For this reasons it was preferred for this application.

In the numerical simulation of the process the problem was discretized in time using an updated Lagrangian approach. The displacement is updated from a given displacement $\mathbf{u}(t)$ and the calculated velocity $\mathbf{v}(t + \Delta t)$ in the following way:

$$\mathbf{u}(t + \Delta t) = \mathbf{u}(t) + \mathbf{v}(t + \Delta t) \Delta t \quad (2.18)$$

the velocities $\mathbf{v}(t + \Delta t)$ are then the only unknowns that are calculated by solving the equilibrium equations with the Direct Iteration Method at each time step. The method is started assuming $\mu = \mu_0$ and then the stiffness matrix at the iteration n is calculated from the values of the previous iteration in the following way:

$$\mathbf{K}_S^n = \sum_{I=1}^{N_N} \tilde{\mathbf{B}}_I^T (\mathbf{E}_{(\mu^{n-1})} - \alpha \tilde{\mathbf{E}}_{(\mu^{n-1})}) \tilde{\mathbf{B}}_I \tilde{V}_I + \alpha \sum_{J=1}^{N_E} \mathbf{B}_J^T \tilde{\mathbf{E}}_{(\mu^{n-1})} \mathbf{B}_J A_J \quad (2.19)$$

once $\mathbf{v}^n = \mathbf{v}^{n-1}$ the iteration is stopped and the values of the velocity are used to update the problem in time and start the following time step.

The model in figure 2.3 was studied assuming a punch speed of $1mm/s$ and considering 50 time steps of $1s$ each. The performances of the NI schemes were

2.3 A comparison between the different NI schemes and their stabilization in the simulation of extrusion

analysed on both the regular and the irregular mesh in figure 2.4, that have about 1000 nodes each. The evolution of the initial cloud of nodes was followed during the simulations without introducing remeshing and the shape of the cloud was determined at each step using the alpha-shape criterion (31).

In figure 2.5 the LV scheme was applied and no stabilization was introduced. Looking at the velocity field of the regular mesh the presence of the spurious modes is clearly observable; the pressure field presents strong oscillations in the direction of the mesh as well. The situation is quite different with the irregular mesh. In this case the velocity field is quite more regular and the pressure field has a satisfactory trend, considering the reduced number of nodes.

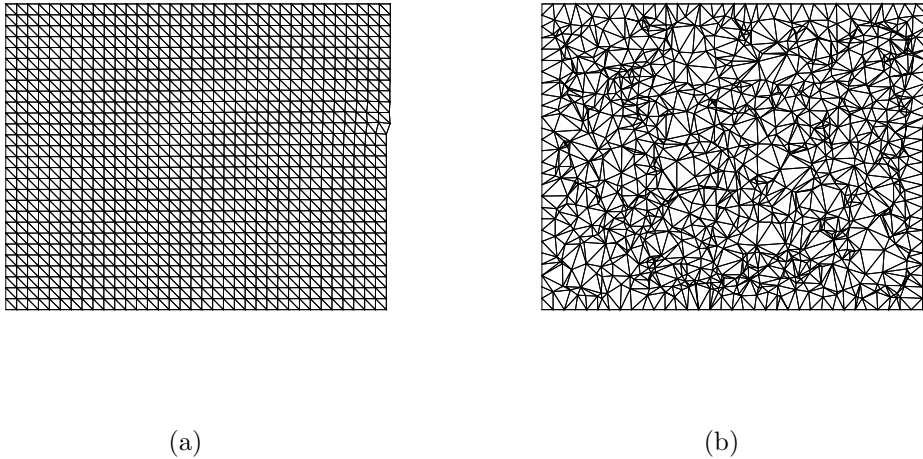


Figure 2.4: The meshes used for the simulation - (a) regular and (b) irregular.

This proves that the nodal integration performs poorly with regular meshes due to the spurious low energy modes, while the irregularity of the mesh gives a partial stabilization to the method. The effect of the stabilizing method proposed in (18) is analysed in figure 2.6 where again the LV scheme was used with both regular and irregular meshes. We can observe that with $\alpha = 0.05$ we already have a significant stabilizing effect and that $\alpha = 0.10$ in this application is enough to have a completely stabilized field, as in a traditional FEM simulation.

2.3 A comparison between the different NI schemes and their stabilization in the simulation of extrusion

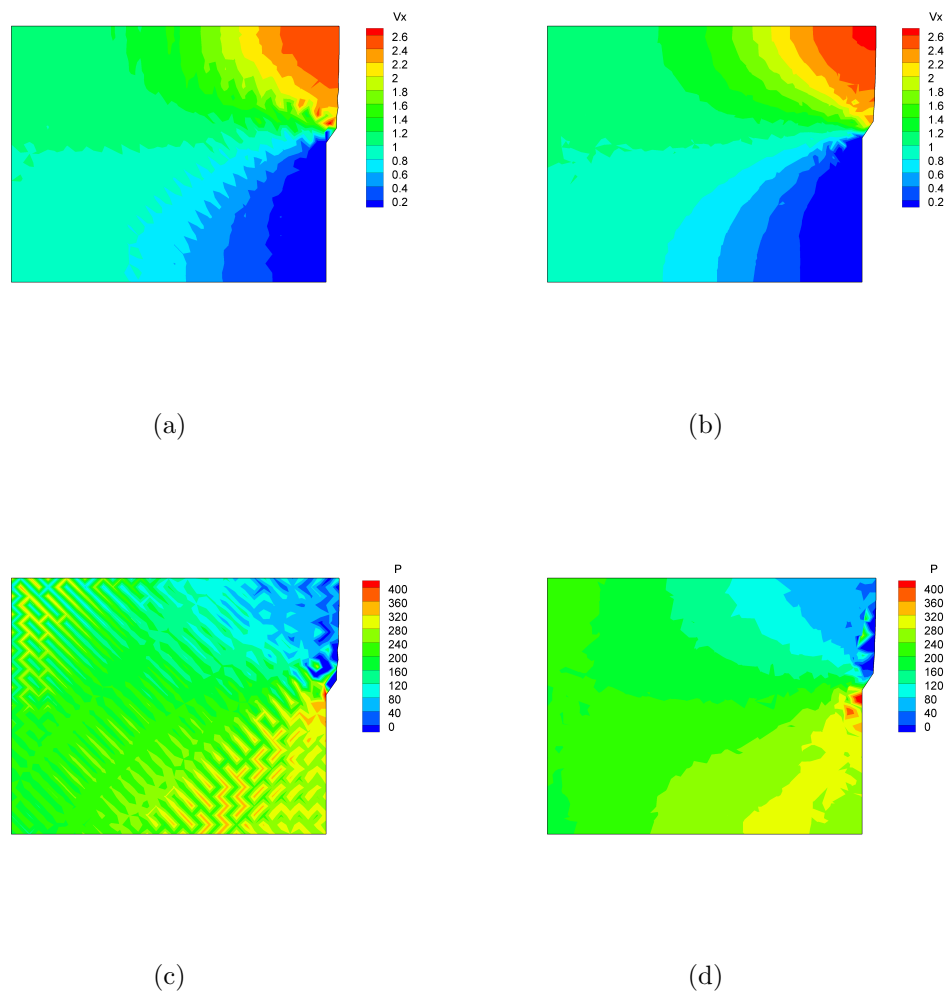
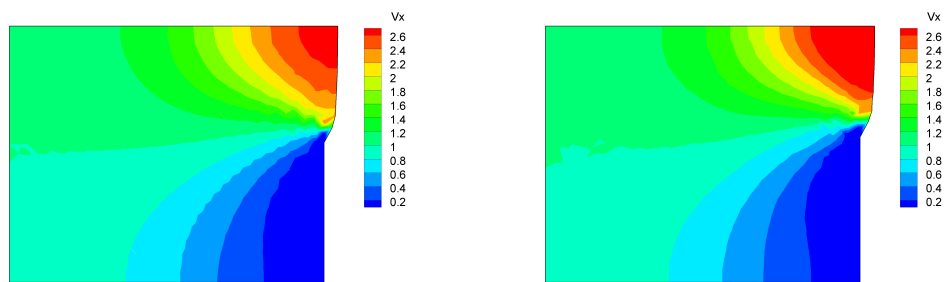


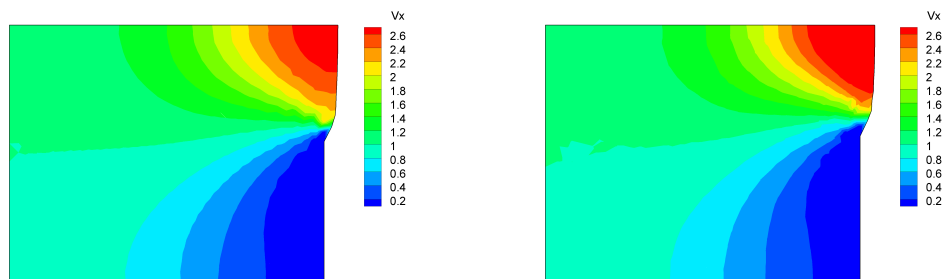
Figure 2.5: The effects of the regularity of the mesh at the beginning of the simulation (no stabilization) - velocity field with a regular (a) and an irregular (b) mesh and pressure field with a regular (c) and an irregular (d) mesh.

2.3 A comparison between the different NI schemes and their stabilization in the simulation of extrusion



(a) Regular mesh, $\alpha = 0.05$

(b) Irregular mesh, $\alpha = 0.05$



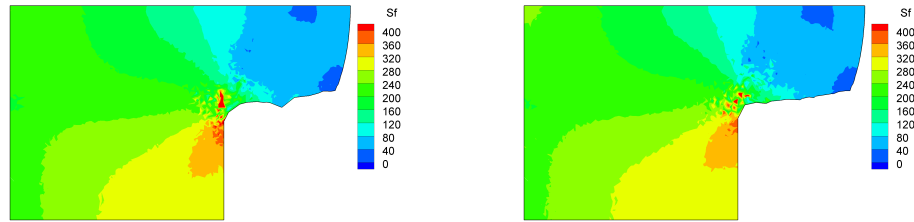
(c) Regular mesh, $\alpha = 0.10$

(d) Irregular mesh, $\alpha = 0.10$

Figure 2.6: The effects of the stabilization on the velocity field

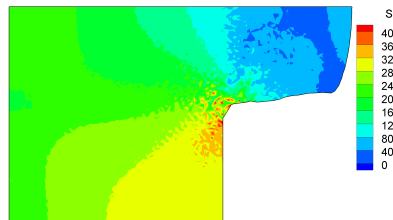
2.3 A comparison between the different NI schemes and their stabilization in the simulation of extrusion

As far as the performances of the different NI schemes are concerned in figure 2.7 we can observe the trend of the flow stress at the end of the simulation, for an irregular mesh of 5000 nodes and without stabilization. In this case the Voronoi-based schemes are quite similar, while the DA presents a slightly lower and more irregular field. Since, according to section 2.2, the DA and LV schemes would be preferable for the computational times and considering the more regular trend of LV results, that are in excellent agreement with the GV ones, the Local Voronoi integration scheme appears the most convenient choice.



(a) GV

(b) LV

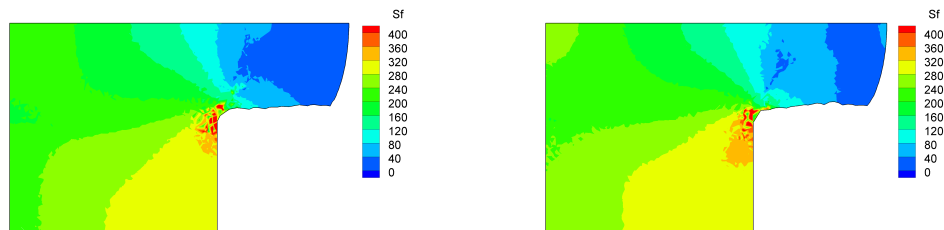


(c) DA

Figure 2.7: The flow stress at the end of the simulation - No stabilization

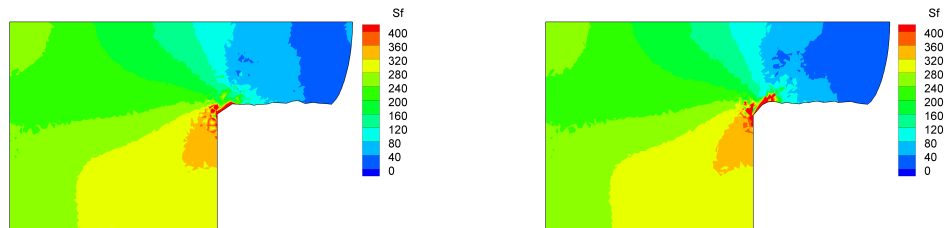
2.3 A comparison between the different NI schemes and their stabilization in the simulation of extrusion

Since no stabilization was considered in figure 2.7 a little error can be observed in the shape of the extruded profile. This is due to the fact that some irregularities are present in the velocity of the nodes that exit from the die. On regularizing such a field with the stabilization (figure 2.8) a better prediction of the shape is obtained.



(a) $\alpha = 0.05$

(b) $\alpha = 0.10$



(c) $\alpha = 0.15$

(d) $\alpha = 0.20$

Figure 2.8: Effects of the stabilization on the stress field - The shape of the extruded profile is improved but some oscillation are still present in the stress field.

However no benefit is given to the regularity of the stress field, that still exhibits some oscillations due to the nodal averaging of the strains. This is perhaps the main limitation of the nodal integration, which improves the performances of the constant strain finite elements from a mathematical point of view but, in doing so, alters the physical foundation of the model. This is more evident observing the DA results, where the strain is averaged only from a numerical prospective and therefore the oscillations are even bigger.

2.4 Simulation of orthogonal cutting

Orthogonal cutting is a typical process where the classical FEM formulation is stressed by the heavy mesh distortions. On the contrary, in the nodal integrated formulation, the quality of the results is not expected to be affected by the deterioration of the mesh. In this section the two approaches have been compared in the simulation of the process outlined in figure 2.9.

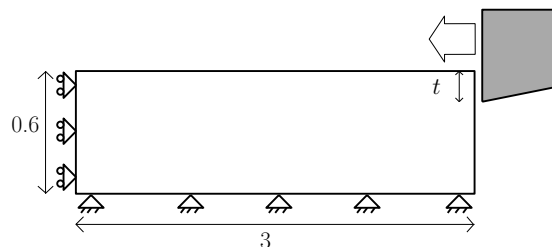


Figure 2.9: Simulation of orthogonal cutting - Sketch of the model.

In order to have a reference FEM result the problem was also studied with the commercial FEM code DEFORMTM.

In the NI simulation the piece was modelled with the cloud of nodes shown in figure 2.10. About 2000 nodes were randomly generated within the work-piece and about 8000 nodes were placed in the cutting zone. Then, during the advancement of the process, no rezoning was applied but, in a very strictly Lagrangian framework, the evolution of the initial cloud of nodes was followed by calculating at each step the alpha-shape of the Delaunay triangulation of the cloud.

2.4 Simulation of orthogonal cutting

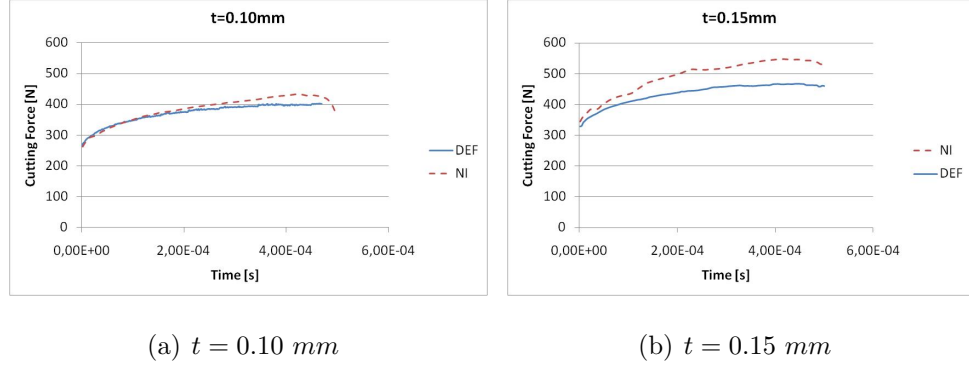


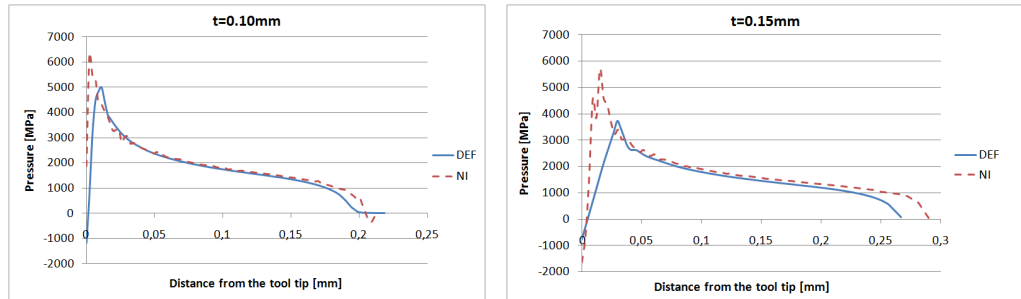
Figure 2.11: The cutting force.

In order to analyse different chip formation dynamics two values of the uncut chip thickness t were considered: 0.10 and 0.15 mm. The cutting speed was 2000 mm/s. For the same reasons outlined in section 2.3 friction and thermal aspects were neglected and the material was described with a Northon-Hoff power law, characterised by $\mu_0 = 50$ and $n = 0.4$, that are typical of common titanium alloys for aerospace applications (30).

An important variable to calculate in the simulation of cutting is the force required to the tool. Although its evaluation does not strongly depend on local phenomena that could affect the code prediction, the cutting force is a relevant variable from an industrial point of view because it is responsible of mechanical stress on the tooling. As it can be observed in figure 2.11, the trends calculated with the two methods are similar but the NI code predicts a slight higher value. The reason of this higher estimation is explained observing the pressure distribution on the rake face in figure 2.12. We can note that the NI code (dashed lines) presents a better simulation capability close to the tool tip. The commercial code, in fact, losses the contacts in this zone and the new equilibrium reduces the pressure on the rake face. In the NI case the nodes are not rezoned and this ensures a better efficiency of the contact algorithm. Since the load depends on the pressure distribution this justifies also the differences in the load predictions.

The quality of the NI prediction is roughly demonstrated also observing the geometries calculated using both the approaches that are simultaneously reported in figure 2.13. Nevertheless the strong simplification in the NI formulation the

2.4 Simulation of orthogonal cutting



(a) $t = 0.10 \text{ mm}$

(b) $t = 0.15 \text{ mm}$

Figure 2.12: The pressure on the rake face.

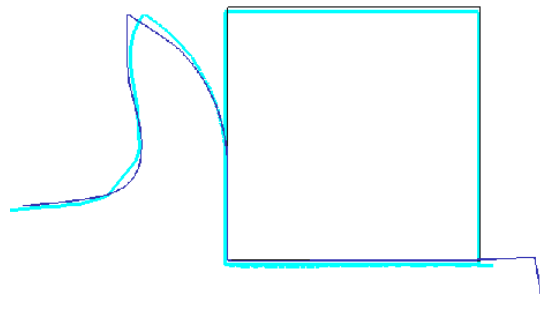


Figure 2.13: The predicted geometry with the two codes - Nodal integrated FEM (shaded line) and DEFORMTM (dark line).

two predicted shapes are very similar. This confirms the overall performance of the NI code since other investigations assessed the quality of the DEFORMTM predictions in cases such the one considered in this example.

3

The *maximum entropy* approximants

3.1 Introduction

After their first introduction in the late seventies meshless methods had a strong development only in the last two decades due to their potentialities in the simulation of several problems not well suited to conventional computational methods (finite elements, finite volume and finite difference methods) such as manufacturing processes like extrusion and moulding, failure propagation problems and simulation of castings.

The starting point of meshless methods is considered to be the Smooth Particle Hydrodynamics (SPH) method (32) that was introduced to model astrophysical phenomena without boundaries such as exploding stars and dust clouds. On introducing a correction function for kernels in the SPH formulation the Reproducing Kernel Particle Methods (RKPM) were later obtained (33, 34).

A parallel path to construct meshless approximants was based on the use of moving least square (MLS) approximations. In (35) the so called Diffuse Element Method (DEM) is presented as an alternative to the conventional FEM in which the MLS approximation is used in a Galerkin method. By refining and modifying the DEM a new class of methods, called Element Free Galerkin Methods (EFGM)

was introduced (36, 37). This class was shown to be consistent and, in the forms proposed, quite stable although substantially more expensive than SPH (14). In (38) the EFG method was further developed and it was proved that the shape functions constitute a partition of unity and that, despite the order of the approximation there is the possibility to enrich these functions in order to make them reproduce a polynomial or arbitrary order. This approach was further generalized to define the so called Partition of Unity Finite Element Method (PUFEM) (39, 40).

As it was shown in (14) the RKPM, the EFGM and the PUFEM share many features of the same framework and, in most cases, MLS methods are identical to kernel methods; in particular any kernel method in which the parent kernel is identical to the weight function of a MLS approximation and is rendered consistent by the same basis is identical.

Thanks to this developments meshless methods come to an age of maturity in the middle nineties and, after then, only two methods with really different characteristics were introduced: the Natural Element Method (NEM) (41, 42, 43) and the *Maximum Entropy* (max-ent) methods. The latter will be introduced in section 3.2 and then some original developments realised in this project will be presented in sections 3.3 and 4 . Finally in chapter 5 their application will be extended to metal forming and cutting problems.

Although MLS based methods acquired a great popularity for some years they still present some notable drawbacks such as the lack of the Kronecker-delta property (i.e., the approximated function does not pass through nodal values) for the imposition of the boundary conditions and the errors related to the numerical integration. In the quest of a method free of interpolation errors along the boundary the NEM was the first successful attempt. It was presented a Galerkin method where interpolation was given by Natural Neighbour methods (44, 45). To compute the NEM basis functions the Voronoi diagram and the Delaunay triangulation (that is its dual structure (23)) are required. Although a triangular mesh is employed the NEM was shown to provide a good accuracy despite the quality or distortion of such a mesh (41, 46). Despite these interesting properties the main drawback of NEM is its high computational cost, especially for Sibson

interpolation (44). However, in non-linear computations, while frequent Newton-Raphson iterations are needed, the relative cost of shape function computation is obscured by the cost of updating tangent stiffness matrices.

As introduced before a very delicate matter to take into account for most of meshless methods is the imposition of the essential boundary conditions (47, 48). This is due to the fact that, because of the inherent unstructured connectivity between nodes in the model, interior nodes could eventually influence the result on the boundary. In general EFGM and RKPM present this problem. A possible solution to deal with this inconvenient that was presented for the EFG methods was simply to couple them with a strip of finite elements close to the the boundary (49). Unfortunately, although it is very simple to implement, this method somehow eliminates the meshless character of the approximation. Other possible techniques rely on constrained variational principles (50), penalty formulations or Lagrange multipliers but, anyway, a true interpolation along the boundary is not achieved.

The situation changes in the NEM case, where the NN basis functions are in general interpolant along convex boundaries and, with some modifications, can be interpolant also on non-convex domains (51, 52).

Another aspect to take into account in the framework of Galerkin implementations of meshless methods is the numerical integration. In fact in general meshless formulations do not employ polynomial shape functions and therefore an error is introduced on employing Gauss quadrature formulas. What is more the integration cells that are required to perform the integration do not generally conform with the support of the basis functions which gives another source of error. Although some strategies are possible to deal with the latter problem (53, 54), the non polynomial character of the approximation remains a source of error that can not be avoided in most methods.

As mentioned in chapter 2 an important advancement in the numerical integration of meshless methods arose with the development of the Stabilized Conforming Nodal Integration scheme (SCNI) (20). In the meshless framework equation 2.5 is modified applying the Gauss's divergence theorem. In this way the displacements substitute the strains in the calculation of the assumed strain and therefore the shape functions are used instead of their derivatives in the numerical

implementation. It is worth to note that this approach is possible in the meshless case due to the smoother character of the basis functions, while in the FEM the reduced support of the shape functions could give too high integration errors.

According to (20) this nodal quadrature scheme has rendered excellent results when applied to EFGM. It looks also very well suited to be applied in the NEM framework, since most of the entities required in the SCNI implementations has to be anyway calculated for the NN basis functions. Another advantage of the SCNI scheme is that it leads to a truly nodal implementation of meshless methods since no recovery of secondary variables nor nodal averaging must be performed.

3.2 The *maximum entropy* approximants

Within the family of meshfree approximation methods, a recent advance in computational mechanics has been the development and application of maximum-entropy (max-ent) based approximation schemes (16, 70, 71, 72). These approximations are linked to elements from information theory (73), convex analysis (74), and convex optimization (75).

Initially, these convex approximants were introduced by Sukumar (70) for constructing polygonal interpolants and by Arroyo and Ortiz (16) for use in meshfree methods. Since then, many new developments and applications of max-ent basis functions have emerged: unifying formulation using relative entropy and an extension to higher-order schemes with signed basis functions (76), quadratically complete convex approximations (77, 78, 79), epi-convergence to establish continuity of max-ent basis functions (80) and convergence analysis of max-ent approximation schemes (81, 82), constructing barycentric coordinates on arbitrary polytopes (83), fluid and plastic flow using optimal transportation theory (84), compressible and nearly incompressible elasticity (85, 86, 87, 88), variational adaptivity for finite-deformation elasticity (89), thin-shell analysis (90, 91), modeling Mindlin-Reissner shear-deformable plates (92), nonlinear structural analyses (93, 94), convection-diffusion problems (95, 96, 97), phase-field model of biomembranes (98, 99), curvature and bending rigidity of membrane networks (100), and Kohn-Sham density functional calculations (101).

3.2 The *maximum entropy* approximants

In information theory (73), the notion of entropy as a measure of uncertainty or incomplete knowledge was firstly introduced by Shannon (102). Then Jaynes proposed the principle of *maximum entropy* (103) in which it was shown that maximizing entropy provides the least-biased statistical inference when insufficient information is available.

Consider a set of distinct nodes in \mathfrak{R}^d that are located at \mathbf{x}_a ($a = 1, 2, \dots, n$), with $\Omega = \text{con}(\mathbf{x}_1, \dots, \mathbf{x}_n) \subset \mathfrak{R}^d$ denoting the convex hull of the nodal set. For a real-valued function $u(\mathbf{x}) : \Omega \rightarrow \mathfrak{R}$, the numerical approximation for $u(\mathbf{x})$ is:

$$u^h(\mathbf{x}) = \sum_{a=1}^n \phi_a(\mathbf{x}) u_a, \quad (3.1)$$

where $\phi_a(\mathbf{x})$ is the basis function associated with node a , and u_a are coefficients. In the maximum-entropy approach an entropy functional that depends on a discrete probability measure $\{p_a\}_{a=1}^n$ is maximized, subject to linear constraints on p_a . On noting the correspondence between basis functions $\{\phi_a\}_{a=1}^n$ and discrete probability measures $\{p_a\}_{a=1}^n$, the max-ent formalism was recently applied to construct basis functions. The idea was firstly introduced by Sukumar for the construction of polygonal interpolants (70). The associated max-ent variational formulation was: find $\mathbf{x} \mapsto \boldsymbol{\phi}(\mathbf{x}) : \Omega \rightarrow \mathfrak{R}_+^n$ as the solution of the following constrained (concave) optimization problem:

$$\max_{\boldsymbol{\phi} \in \mathfrak{R}_+^n} - \sum_{a=1}^n \phi_a(\mathbf{x}) \ln \phi_a(\mathbf{x}), \quad (3.2)$$

subject to the linear reproducing conditions:

$$\sum_{a=1}^n \phi_a(\mathbf{x}) = 1, \quad (3.3a)$$

$$\sum_{a=1}^n \phi_a(\mathbf{x})(\mathbf{x}_a - \mathbf{x}) = \mathbf{0}, \quad (3.3b)$$

where \mathfrak{R}_+^n is the non-negative orthant, and the linear constraints form an underdetermined system. The aforementioned approach is suitable for polygonal meshes, where the max-ent basis functions are calculated in each polygon but can not be directly applied to scattered clouds of nodes because too many nodes would have influence in the calculations.

3.2 The *maximum entropy* approximants

In order to extend the max-ent approach to the application in meshfree implementations in (16) they tried to modify the character of the basis functions introducing a Pareto optimum between the maximization of the entropy and their locality. Firstly they noted that, according to (104), the piecewise affine shape functions defined on the Delaunay triangulation of a set of nodes can be obtained through convex optimization by solving the following minimization problem

$$\min_{\phi \in \mathbb{R}_+^n} \sum_{a=1}^n \phi_a(\mathbf{x}) |\mathbf{x} - \mathbf{x}_a|^2, \quad (3.4)$$

subject to the linear reproducing constraints given by equation 3.3. Since the total width is minimized these shape functions are the most local possible functions for a given cloud of nodes. Therefore they propose to modify the max-ent formulation by introducing a Pareto optimum between eq. 3.4 and eq. 3.2. In particular the following optimization problem is solved:

$$\min_{\phi \in \mathbb{R}_+^n} \sum_{a=1}^n \beta_a \phi_a(\mathbf{x}) |\mathbf{x} - \mathbf{x}_a|^2 + \sum_{a=1}^n \phi_a(\mathbf{x}) \ln(\phi_a(\mathbf{x})) \quad (3.5)$$

always subject to the constraints in eq. 3.3. The basis functions obtained with this scheme are known in the literature as *local maximum entropy* (LME) approximants. The Pareto parameter β_a controls the locality of the basis function of each node. In particular the functions become more local when β_a increases until the case of $\beta_a \rightarrow \infty$ where the Delaunay shape functions are recovered. On the contrary for $\beta_a = 0$ purely max-ent basis functions are obtained. This behaviour is illustrated in Figure 3.1 for a one-dimensional domain. Since the influence of β depends on the mesh size normally a non-dimensional parameter $\{\gamma_a = \beta_a h_a^2\}_{a=1, \dots, N}$ is preferred. Typical values of γ used in the reference applications are in the range from 0.8 to 1.6.

In a more recent development (76) Sukumar proposed, as a generalization, to substitute Shannon entropy in equation 3.2 with the Shannon-Jaynes entropy measure (105), also known as relative entropy. The resulting optimization problem is then

$$\max_{\phi \in \mathbb{R}_+^n} - \sum_{a=1}^n \phi_a(\mathbf{x}) \ln \left(\frac{\phi_a(\mathbf{x})}{w_a(\mathbf{x})} \right), \quad (3.6)$$

3.2 The *maximum entropy* approximants

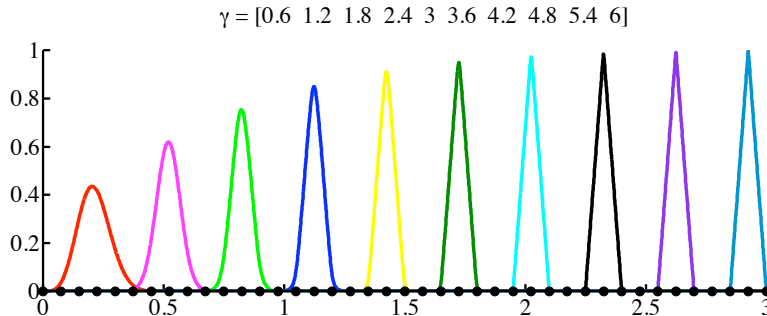


Figure 3.1: Seamless and smooth transition from meshfree to Delaunay affine basis functions. The transition is controlled by the non-dimensional nodal parameters γ_a , which here take linearly varying values from 0.6 (left) to 6 (right).

subject to the constraints in eq. 3.3. In this expression $w_a(\mathbf{x}) : \Omega \rightarrow \mathfrak{R}_+$ is a non-negative weight function that is called *prior estimate* to ϕ_a . Different max-ent basis functions can then be obtained depending on the choice of the prior. We can note that for $w_a(\mathbf{x}) = 1 \forall a$ the global max-ent approximants are recovered, while choosing $w_a(\mathbf{x}) = \beta_a |\mathbf{x} - \mathbf{x}_a|^2$ due to the property of the logarithm operator equation 3.6 recovers the LME formulation. Although many different approximants can be obtained with this formulation the LME basis functions have been preferred in all the numerical applications (see aforementioned references) due to their properties and to the facility of their implementation.

On using the method of Lagrange multipliers, the solution of the variational problem in eq. 3.6 is (76):

$$\phi_a(\mathbf{x}) = \frac{Z_a(\mathbf{x}; \boldsymbol{\lambda})}{Z(\mathbf{x}; \boldsymbol{\lambda})}, \quad Z_a(\mathbf{x}; \boldsymbol{\lambda}) = w_a(\mathbf{x}) \exp(-\boldsymbol{\lambda} \cdot \tilde{\mathbf{x}}_a) \quad (3.7)$$

where $\tilde{\mathbf{x}}_a = \mathbf{x}_a - \mathbf{x}$ ($\mathbf{x}, \mathbf{x}_a \in \mathfrak{R}^d$) are shifted nodal coordinates, $\boldsymbol{\lambda}(\mathbf{x}) \in \mathfrak{R}^d$ are the d Lagrange multipliers associated with the constraints in eq. 3.3b, and $Z(\mathbf{x})$ is known as the *partition function* in statistical mechanics. On considering the dual formulation, the solution for the Lagrange multipliers can be written as (75)

$$\boldsymbol{\lambda}^* = \operatorname{argmin} F(\boldsymbol{\lambda}), \quad F(\boldsymbol{\lambda}) := \ln Z(\boldsymbol{\lambda}), \quad (3.8)$$

where $\boldsymbol{\lambda}^*$ is the optimal solution that is desired. Since F is strictly convex in the interior of Ω , a convex optimization algorithm such as Newton's method is used to determine $\boldsymbol{\lambda}^*$.

3.3 Derivatives of max-ent basis functions on the boundary of the domain

Let $\phi_a^*(\mathbf{x})$ be the max-ent basis function that corresponds to the converged $\boldsymbol{\lambda}^*(\mathbf{x})$, and $\nabla\phi_a^*(\mathbf{x})$ and $\nabla\nabla\phi_a^*(\mathbf{x})$ be the gradient and Hessian of $\phi_a^*(\mathbf{x})$, respectively. We obtain $\phi_a^*(\mathbf{x})$ from eq.3.7:

$$\phi_a^*(\mathbf{x}) = \frac{Z_a(\mathbf{x}; \boldsymbol{\lambda}^*)}{Z(\mathbf{x}; \boldsymbol{\lambda}^*)}, \quad Z_a(\mathbf{x}; \boldsymbol{\lambda}^*) = w_a(\mathbf{x}) \exp(-\boldsymbol{\lambda}^* \cdot \tilde{\mathbf{x}}_a). \quad (3.9)$$

The gradient of $\phi_a^*(\mathbf{x})$ for the LME prior is presented in (16), and that for an arbitrary prior weight function appears in References (93, 106). The latter is reproduced below:

$$\begin{aligned} \nabla\phi_a^* &= \phi_a^* \{ \tilde{\mathbf{x}}_a \cdot [(\mathbf{H}^*)^{-1} - (\mathbf{H}^*)^{-1} \cdot \mathbf{A}^*] \\ &- \sum_{b=1}^n \frac{\nabla w_b \exp(-\boldsymbol{\lambda}^* \cdot \tilde{\mathbf{x}}_b)}{Z} + \frac{\nabla w_a \exp(-\boldsymbol{\lambda}^* \cdot \tilde{\mathbf{x}}_a)}{Z} \end{aligned} \quad (3.10a)$$

where

$$\mathbf{H}^* = \sum_{b=1}^n \phi_b^* \tilde{\mathbf{x}}_b \otimes \tilde{\mathbf{x}}_b, \quad \mathbf{A}^* = \sum_{b=1}^n \tilde{\mathbf{x}}_b \otimes \frac{\nabla w_b \exp(-\boldsymbol{\lambda}^* \cdot \tilde{\mathbf{x}}_b)}{Z} \quad (3.10b)$$

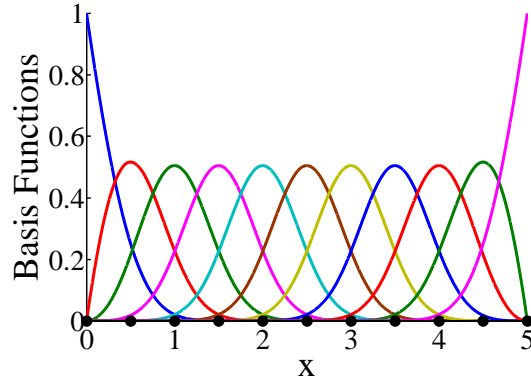
The derivation and expression for the Hessian of $\phi_a^*(\mathbf{x})$ is presented in References (79, 100, 106). In figure 3.2 the LME basis functions are plotted together with their derivatives on a one-dimensional domain uniformly discretized and using a dimensionless parameter $\gamma = 0.8$.

LME approximants are endowed with features such as monotonicity, smoothness and variation diminishing property, as illustrated in Figure 3.3. They also satisfy *ab initio* a weak Kronecker-delta property at the boundary of the convex hull of the nodes. With this property, the imposition of essential boundary conditions in Galerkin methods is straightforward. Moreover, the approximants are multidimensional and lead to well behaved mass matrices.

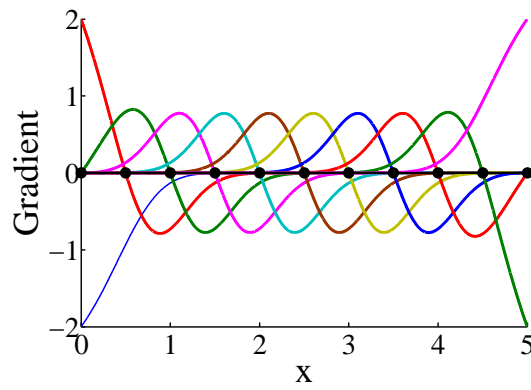
3.3 Derivatives of max-ent basis functions on the boundary of the domain

As noted in References (70) and (16), the Lagrange multipliers blow up for a point $\mathbf{x} \in \partial\Omega$, and hence the expressions derived therein for $\nabla\phi_a$ can not be used

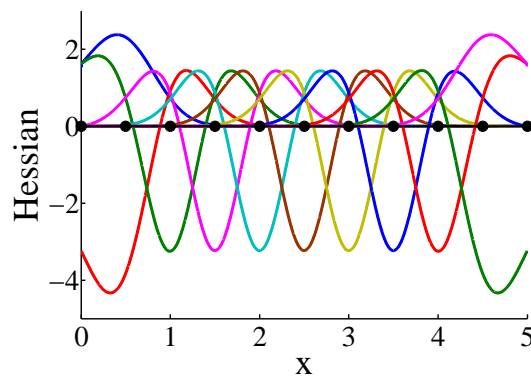
3.3 Derivatives of max-ent basis functions on the boundary of the domain



(a)



(b)



(c)

Figure 3.2: One-dimensional local maximum-entropy basis functions (a), and its first (b) and second (c) derivatives, computed with a dimensionless parameter $\gamma = 0.8$.

3.3 Derivatives of max-ent basis functions on the boundary of the domain

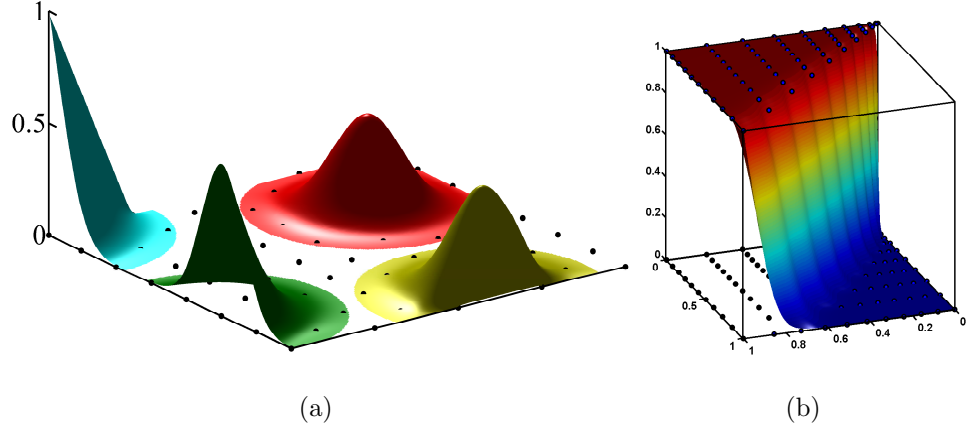


Figure 3.3: Illustration of non-negativity, smoothness and weak Kronecker-delta properties for two-dimensional local maximum-entropy basis functions (a), and the variation diminishing property (b).

to evaluate the derivatives of the basis functions on the boundary. As an original contribution of this project, a solution for this problem is provided in (107). In particular the l'Hôpital's rule is applied to obtain explicit expressions for the derivatives of the basis functions on the boundary, which is guided by theoretical analysis and supportive numerical experiments. Furthermore, on choosing appropriate *prior* weight functions, a means to obtain bounded Lagrange multipliers on the boundary is presented, which leads to bounded first- and higher-order derivatives of max-ent basis functions on $\partial\Omega$. In addition, in (107), optimal convergence rates for Euler-Bernoulli beam problems and for plate bending problems are demonstrated for a Galerkin approach with a quadratically complete partition-of-unity enriched max-ent approximation.

4

Blending between isogeometric and max-ent approximants

4.1 Introduction

In the last years a lot of research has been carried out in the field of Isogeometric Analysis (IGA) (108, 109), a technique that aims at integrating the Computer Aided Design (CAD) with the FE analysis by parameterizing the domain and discretizing the PDE with the same basis functions, e.g. B-Splines or NURBS. In this way the exact CAD geometry is preserved and, what is more, the two processes of CAD design and FE analysis can be integrated not only in the sense of using the same software (all the reference CAD software includes finite element tools) but also in the mathematical approach to the two operations.

The main drawback arising from this technique is that the NURBS framework imposes some rigidity on volume meshing, which requires special technologies to accommodate trimmed surfaces, local refinement, or incongruent surface descriptions at opposing faces (110, 111, 112, 113, 114, 115, 116). On the contrary the max-ent approximants present more flexibility and easily handle volume discretization and unstructured grids but possess the inherent limitation of meshfree methods to represent complex boundaries with high fidelity. In fact, the only boundaries that can be represented by a mere collection of points are polytopes,

either the convex hull or more controllable domains like the alpha shapes (31). In addition the Kronecker-delta property of LME approximants does not hold on non-convex boundaries (16). This fact suggests that limitations of IGA and LME approximants are in some sense complementary.

For this reasons, recently the IGA-LME approximants were proposed (17). The idea of this method is to use isogeometric functions to parametrize the boundary of the domain and, introducing a thin layer of control points, to construct the approximants for the nodes that lead on it. The basis functions of the internal nodes are calculated using the standard LME formulation, while in the parametrized domain a blending between the isogeometric basis functions and the basis functions of the internal nodes is realized using a modified maximum entropy approach. In this way any arbitrary shape can be described without loss of precision on the boundary and, at the same time, without the limitations given by the isogeometric representation, since it is required only on a thin zone.

4.2 The IGA-LME formulation

When the IGA-LME approach is employed, focusing on 2D for simplicity, the boundary of the domain $\partial\Omega$ is parameterized with a B-Spline curve Γ (Fig. 4.1a), which is obtained trough a function $C : [\xi_1, \xi_2] \mapsto \Gamma$ defined as:

$$C(\xi) = \sum_i M_i(\xi)P_i, \quad (4.1)$$

where $M_i(\xi)$ are the one dimensional basis functions calculated on a knot span in the interval $[\xi_1, \xi_2]$ (Fig. 4.1b), and $P_i \in \mathbb{R}^2$ are the control points. In figure 4.1 as well as in (17) cubic B-Spline functions (order $p = 3$) are used. However, the method can be implemented also with different values of p .

In the IGA-LME formulation a ring of isogeometric basis functions associated with the boundary nodes is then defined in a subset Ω_\star of the two dimensional computational domain Ω (see Fig. 4.1a). For this purpose an isogeometric mapping $S : [\xi_1, \xi_2] \times [\eta_1, \eta_2] \mapsto \Omega_\star$ is defined as

$$S(\xi, \eta) = \sum_i \sum_j M_i(\xi)P_j(\eta)P_{i,j}. \quad (4.2)$$

where $P_j(\eta)$ are again one dimensional basis functions calculated on a knot span in the interval $[\eta_1, \eta_2]$ (Fig. 4.1c). Associating to each point $\mathbf{x} = S(\xi, \eta)$ the value $N_b(\mathbf{x}) = M_i(\xi)P_1(\eta)$ the two dimensional basis functions are obtained in Ω_\star (blue function in Fig. 4.1d). In the example in the figure, since cubic B-Splines are used, other three internal rings of control points are needed to define $S(\xi, \eta)$.

At this point the blending with the LME approximants is realized in Ω_\star by including the B-spline basis functions associated to the control points on the boundary in the constraints of the *maximum entropy* optimization problem that becomes

$$\begin{aligned}
 &\text{For fixed } x \text{ minimize} && \sum_{a \in \mathcal{J}_{ME}} m_a(x) \ln m_a(x) + \sum_{a \in \mathcal{J}_{ME}} \beta_a m_a(x) |x - x_a|^2 \\
 &\text{subject to} && m_a(x) \geq 0, \quad a \in \mathcal{J}_{ME} \\
 &&& \sum_{a \in \mathcal{J}_{ME}} m_a(x) + \sum_{b \in \mathcal{J}_{BS}} N_b(x) = 1 \\
 &&& \sum_{a \in \mathcal{J}_{ME}} m_a(x) x_a + \sum_{b \in \mathcal{J}_{BS}} N_b(x) x_b = x,
 \end{aligned} \tag{4.3}$$

where $m_a(x)$ represents the blended approximants (dark green function in Fig. 4.1d), indicated with \mathcal{J}_{ME} so that the global set of indices $\{1, 2, \dots, N\}$ is given by $\mathcal{J}_{BS} \cup \mathcal{J}_{ME}$. This algorithm is employed for all the nodes that leads in the blending zone, while for all the internal nodes a standard *maximum entropy* procedure is used.

4.3 Numerical Integration

In the purely isogeometric formulation (108) the numerical integration is realized in the parametric domain, as for isoparametric finite elements. On the contrary in the meshfree environment the quadrature is realized directly in the physical space, normally using a background integration mesh. On coupling the two methods different approaches can be employed.

Consider for sake of clarity the circular domain of Fig. 4.1. In (17) the integration is realized in the physical space for both the purely meshless and the blending zone. In this part of the domain an inverse mapping is required to

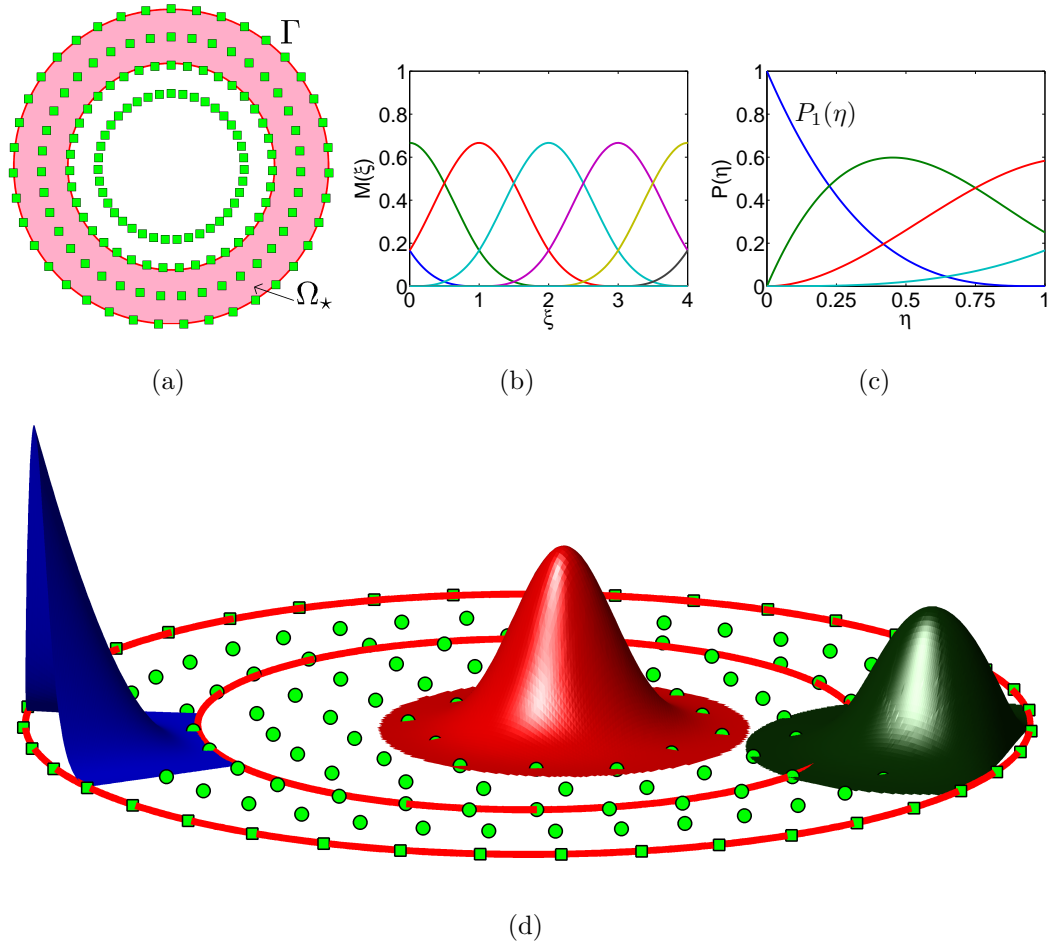


Figure 4.1: IGA-LME blending for a circular domain. (a) The four rings of control points (green squares) that together with B-Spline basis function are used to define the blending zone, circumscribed between the two red lines. (b) The B-Spline basis function in the radial direction. (c) The B-Spline basis function in the tangential direction for the first 5 knots. (d) The three types of basis functions; the blue is fully isogeometric, it is associated to a control point on the boundary and its supports corresponds to the blending zone; the dark green is a blended function associated to a node in such zone and the red is a fully LME basis function. Note that the three internal rings of control points are used only to compute the B-spline basis functions associated to the external ring and then the blending zone is populated with the nodes (green circles) that are used for the computation of the basis functions.

compute the value of the basis functions and their derivatives in the quadrature points. In fact, while it is straightforward to project a point from the parametric to the physical space, the inverse problem $(\xi, \eta) = S^{-1}(x)$ requires the resolution of a non linear set of equations. This increases the computation times and requires supplementary implementation efforts because since the B-Spline functions have a limited support the resolution of the equations with the Newton method is not straightforward.

For this reasons, as an original contribution of this project, the integration in the blending zone has been performed directly in the parametric space. Thus, like in the FEM formulation, the derivatives of the basis functions in the physical space are related to the derivatives in the parametric space using the Jacobian matrix

$$J(\xi) = \sum_i \sum_j P_{i,j} \otimes \nabla N_{i,j}(\xi)$$

and the determinant of J is included into the integrals to take into account the ratio between the areas. The quadrature points are fixed in the parametric space using a Gauss Legendre tensor product rule. For a given number of quadrature points n_p there will be n_p points in the radial direction and n_p points in each interval between two knots in the tangential direction. On using such approach a second mesh is required to complete the integration in the physical space. This mesh is generated using as external nodes the image of the knots in the internal border of the blending zone (Fig. 4.2b)). Note that this mesh is used only to generate the Gauss points in the physical domain, while the nodes are given by the primary mesh. This mesh can be generated by using as external nodes either the first or the second ring of control points. The latter approach is preferable because it ensures that the second ring of nodes has the properly distance from the first one. In fact the feasibility of the computation of LME basis functions in the merge zone depends on the regularity of the distribution of the nodes.

In using the aforementioned integration scheme an error is introduced in the zone where the parametric domain ends and the internal mesh is used for the integration. The error is due to the fact that the mesh cannot exactly reproduce the curvature of the parametric domain and hence some contribution is missed in the integration. In (17) this problem is avoided in the internal border of the

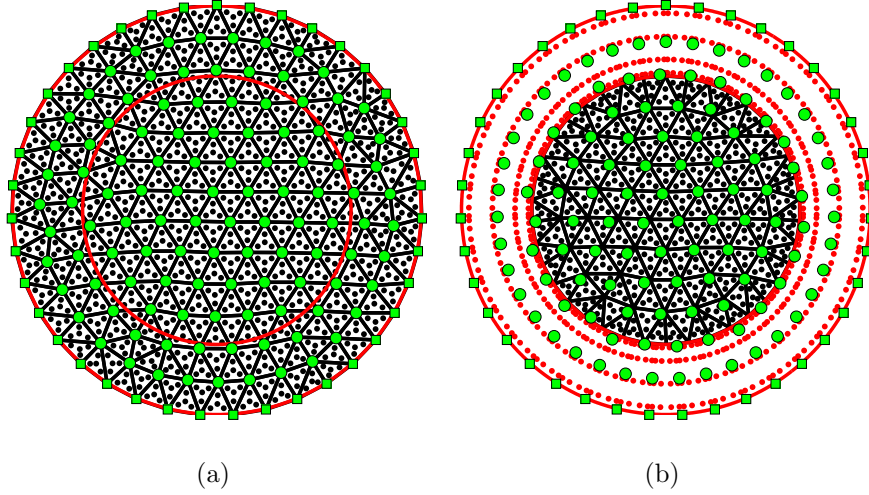


Figure 4.2: Numerical integration. In (17) the mesh is generated with the external ring of control points (green squares) and it is used for the integration and for the computation of the basis functions (a). With the new approach proposed in this project in the blending zone the integration is realized directly in the parametric domain. The red points represent the projection of the integration points in the physical domain. Then the black mesh is used to generate the integration points (in black) in the rest of the physical domain. The nodes (green circles) are generated independently (b) .

parametric zone but it is present on the external border of the domain. In fact, also in this case, the mesh used for the computation of the nodes and for the integration cannot exactly reproduce the curvature of the domain. In addition the influence of the error is more relevant in this zone, where the IGA-LME approach is supposed to give a higher geometric precision. For this reason in (17) the integration in the boundary cells is realized using quadrature rules for high order curved elements. On the contrary, with the new strategy proposed herein, the error due to the curvature is limited to a zone where its influence is less significant and therefore a standard approach can be used for the quadrature; at the same time the performances of the method are improved since the reverse mapping is avoided.

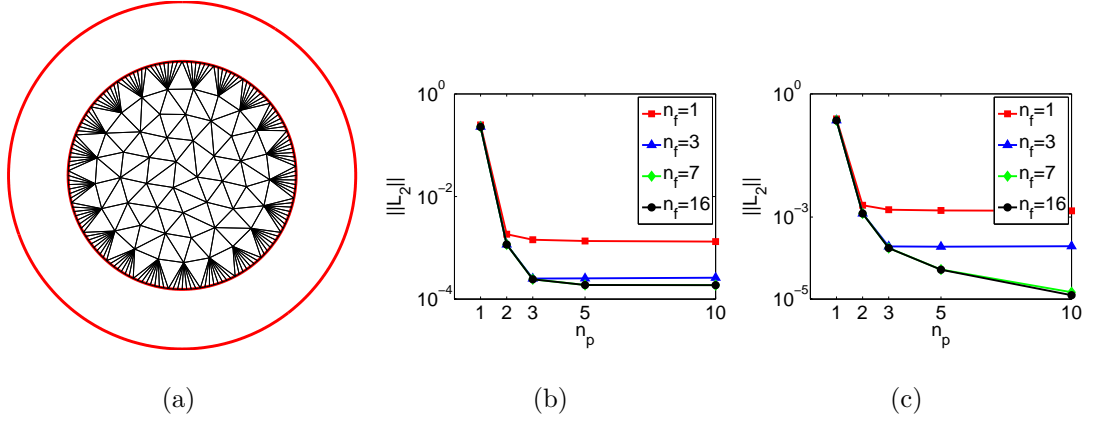


Figure 4.3: The linear elasticity patch test. (a) The refined integration mesh ($n_r = 4$); (b) the L_2 norm of the relative error without refinement; (c) the L_2 norm of the relative error with refinement.

To confirm the accuracy of this approach the linear elasticity patch test has been considered for the domain in Fig. 4.2b. With the proposed integration strategy three seeds of error are present:

- the integration in the parametric space for the blending zone
- the integration in the internal mesh
- the error due to the curvature

The influence of the latter can anyway be reduced by the mesh refinement. As illustrated in Fig. 4.3a in the generation of the internal mesh a higher number of virtual nodes can be used in order to reduce the influence of the curvature. This refinement is applied only to the external triangles, while in the internal part a mesh size coherent with the nodal spacing is used. We define n_r as the number of virtual nodes, for each knot interval, used in the generation of the internal mesh. Therefore the original mesh has $n_r = 1$ while the mesh in Fig. 4.3a has $n_r = 4$.

To study the error in the patch test the following linear transformation has been imposed to the boundary of the domain:

$$\begin{pmatrix} u \\ v \end{pmatrix} = \begin{pmatrix} 1 \\ 1 \end{pmatrix} + \begin{pmatrix} 1 & 0.5 \\ -1 & 0.5 \end{pmatrix} \times \begin{pmatrix} x \\ y \end{pmatrix}$$

The integration was realized using a $n_p \times n_p$ tensor product rule in the parametric space, with $n_p = \{1, 2, 3, 5, 10\}$ while in the rest of the physical space four of the first five Dunavant's quadrature rules (117), with a number of points $n_f = \{1, 3, 7, 16\}$, were used in the triangles of the integration mesh. In Fig. 4.3 we can see the relative error in the L_2 norm in function of n_p and for different values of n_f , using $n_r = 1$ and $n_r = 4$. We can note that for each value of n_r there is a limit of the value of the error that cannot be improved increasing the number of Gauss points. However when n_r is increased a higher number of Gauss points allows to further reduce the error. The values that we found in the refined mesh are not far from those reported on (16) ($\sim 10^{-6}$). Anyway we can note that the value of 2×10^{-4} that is obtained with $n_r = 1$ is already acceptable for most of the practical applications.

4.4 Simulation of contact problems

The simulation of contact problems is still a challenge in several engineering applications due to the high non-linearity intrinsically involved in the phenomenon. The use of FEM or alpha-shapes meshless methods cannot avoid a geometrical error in the reproduction of the boundary which reduces the accuracy of the simulations. On the other hand the isogeometric approach allows us to overcome to this problem by giving a correct representation of the geometries and a more straightforward imposition of the contact constraints. What is more thanks to the coupling with LME approximants the method becomes more flexible and can reproduce arbitrary geometries. For this reasons the IGA-LME approach appears suitable for the simulation of metal forming and manufacturing processes, where the correct simulation of the interaction between the work-piece and the die or the tools can improve the performance of the numerical analysis. Therefore, as an original contribution of this project the IGA-LME formulation has been applied to the simulation of contact problems. In particular some benchmark small deformation contact problems in linear elasticity has been considered. In the following the relative formulation is presented. Then three numerical examples are shown. In all the applications a plain strain state, with $E = 1$ and $\nu = 0.3$, is assumed.

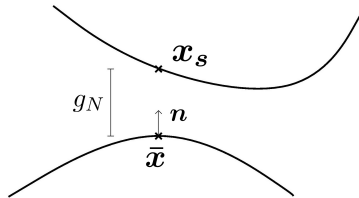


Figure 4.4: The master and the slave surfaces and the gap function.

4.4.1 Formulation

According to (118) the contact between two bodies is simulated by defining a master and a slave surface and imposing the constraints to the points on the slave surface with respect to the master. In particular, for a given point \mathbf{x}_s on the slave surface, a gap function is defined as the distance between \mathbf{x}_s and the closest point on the master surface $\bar{\mathbf{x}}$:

$$g_N = (\mathbf{x}_s - \bar{\mathbf{x}}) \cdot \mathbf{n} \quad (4.4)$$

where \mathbf{n} is the (unit) normal to the master surface in $\bar{\mathbf{x}}$ (Fig. 4.4). Then the so called Signorini condition (?) is imposed in the formulation of the elastic problem:

$$\nabla \cdot \boldsymbol{\sigma} = \bar{\mathbf{f}} \text{ in } \Omega \quad (4.5a)$$

$$\mathbf{u} = \bar{\mathbf{u}} \text{ in } \Gamma_d \quad (4.5b)$$

$$\boldsymbol{\sigma} \cdot \mathbf{n} = \bar{\mathbf{t}} \text{ in } \Gamma_\sigma \quad (4.5c)$$

$$g_N \geq 0, \quad p_N \leq 0, \quad p_N g_N = 0 \text{ in } \Gamma_c \quad (4.5d)$$

where $p_N = \mathbf{t} \cdot \mathbf{n}$ is the normal component of the traction vector. On discretizing the aforementioned equations the inequality $g_N \geq 0$ is included into the integral formulation of the problem. For this purpose the most used methods are the Lagrange multipliers, penalty formulations or combinations of both. Independently of the method that is used a spatial discretization is required to evaluate the contact integral. In the FEM environment several strategy have been studied such the node to segment (NTS) approach, where the contact integral is collocated to enforce the contact condition between a node on the slave surface and an

edge of the master, the segment to segment (STS) approach, where the contact condition is enforced in an integral manner and other classes of spatial discretizations with integrally formulated contact constraints based on the mortar method, surface smoothing algorithms etc. When the isogeometric representation of the boundary is used the NTS technique can be applied without the drawbacks that appear in standard Lagrange polynomials finite elements (119). Furthermore the implementation of the method is straightforward for small deformation contact problems in linear elasticity. In fact the discretized variational formulation consists in:

$$\text{minimize } \frac{1}{2} \mathbf{d}^T \mathbf{K} \mathbf{d} \tag{4.6a}$$

$$\text{subject to } g_N^i \geq 0, \quad i = 1, \dots, n_{coll} \tag{4.6b}$$

where \mathbf{K} is the stiffness matrix, \mathbf{d} the unknowns vector (that for meshfree methods does not correspond to the nodal displacements) and g_N^i are the contact constraints evaluated in each collocation point. In (119) the proper choice of the collocation points is discussed. In particular some problems arise when non-periodic B-splines are used and the contact integrals have to be evaluated close to the boundary of the 1d isogeometric patch. In the applications shown in the following, since the integrals are evaluated far away from such boundary, good results are achieved by choosing the collocation points in correspondence of the knots.

Once the stiffness matrix and the constraint inequalities are calculated eq. 4.6 can be directly solved with a quadratic optimization code.

4.4.2 Hertz's cylinders problem

The Hertz's problem are a typical benchmark in the linear elasticity contact mechanics. In this example the problem of the two cylinders with parallel axes that are forced in contact by a force concentrated on their top has been considered. In the hypothesis of small deformations the normal pressure on the contact zone is given by:

$$p = p_{max} \sqrt{1 - \frac{y^2}{b^2}}, \tag{4.7}$$

4.4 Simulation of contact problems

where b is the length of the contact interface and p_{max} the maximum pressure, that if E and ν are the elastic parameters of the cylinders, R their radius and P/l the force per unit length is given by

$$p_{max} = \sqrt{\frac{1}{\pi(1-\nu^2)} \frac{P E}{l R}}. \quad (4.8)$$

In the numerical solution the contact force can be calculated starting from the values of the Lagrange multipliers in the collocation points. Here the approach presented in (119) has been recovered. In particular for each control point a contact force is extrapolated from the multipliers using the basis functions

$$P_i = \sum_{j=1}^{n_{coll}} N_i(\xi_j) \lambda_j, \quad (4.9)$$

where N_i is the value of the B-Spline basis function of node i and λ_j the value of the Lagrange multiplier in the collocation point j . Then, exploiting the partition of unit property, a nodal length is defined as

$$\ell_i = \int_{\xi_1}^{\xi_2} N_i dl(\xi), \quad (4.10)$$

where $l(\xi)$ is the position on the boundary of the domain. The nodal contact stress σ_i is therefore given by

$$\sigma_i = \frac{P_i}{\ell_i}$$

Finally, respect to (119), in this application the B-Spline basis functions has been employed to obtain a smooth stress distribution on the contact interface:

$$\sigma(l) = \sum_{i=1}^n N_i(l) \sigma_i.$$

The cloud of nodes used for the discretization of the problem is represented in Fig. 4.5a. The density of nodes has been increased in the contact zone. In Fig. 4.5b we can observe how the values of the contact pressure, calculate form the Lagrange multipliers (Fig. 4.5d) are in good agreement with the Hertz's analytical solution. Thanks to the smoothness of the shape functions a very regular trend of the stress is obtained (4.5e). Furthermore with the isogeometric representation of the boundary a very good reproduction of the shape of the surfaces involved in the contact is obtained (4.5c).

4.4 Simulation of contact problems

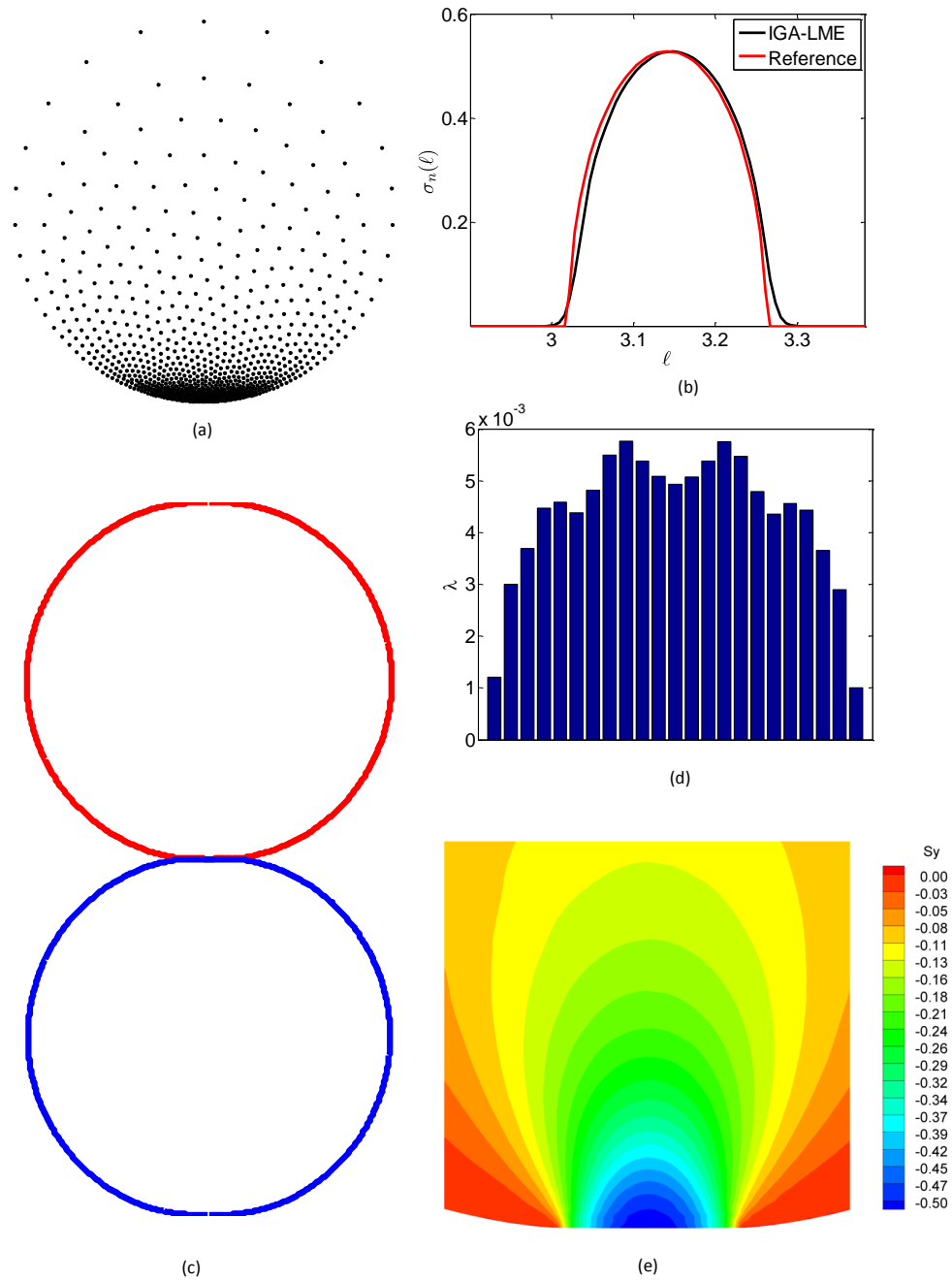


Figure 4.5: Simulation of the Hertz's problem of the two cylinders; (a) the clouds of nodes; (b) the normal stress along the boundary; (c) the deformation of the two cylinders; (d) the Lagrange multipliers in the collocation points; (e) the σ_y stress in the contact zone;

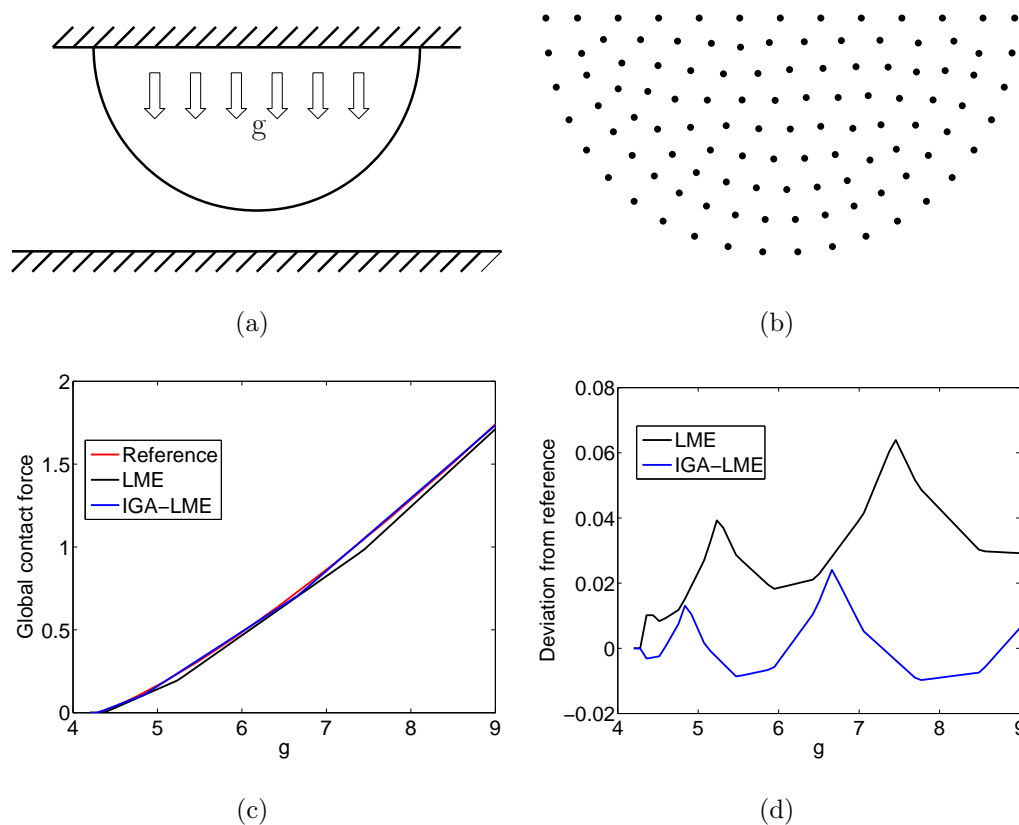


Figure 4.6: Contact of semicircular indenter with a rigid surface; (a) outline of the problem; (b) the cloud of nodes of the IGA-LME simulation; (c) the global contact force in function of the gravity and (d) the relative error respect to a reference solution calculated with a refined mesh. Note how the standard meshless simulation is outperformed by the IGA-LME approach.

4.4.3 Contact of a semi-circular indenter

In order to study the improvement of the accuracy of the method respect to a standard meshless formulation the problem outlined in Fig. 4.6(a) has been also considered. A semicircular domain ($r = 1$) is forced by the gravity to enter in contact with a rigid surface. The problem has been studied using both the IGA-LME and a purely LME approach. In the latter case the contact constrains has been collocated in correspondence of the external nodes with a NTS approach.

In the previous application and in all the problems studied in (17) the whole boundary is parametrized with a periodic B-Spline curve. With this approach the discontinuity between the circular and the straight line on the top of the domain cannot be reproduced unless non uniform knot vectors are used. In addition the isogeometric parametrization is actually required only on the zones of the boundary involved in the contact. Therefore, in this case, the semicircular arc was parameterized with B-spline functions defined on a non periodic knot vector and standard LME interpolants were employed for the top of the domain.

A mesh size of 0.15 was employed for the two simulations. The IGA-LME cloud of nodes is plotted in Fig. 4.6b. When the gravity is increased the semicircle enters in contact with the surface, that reacts with a force. The global value of this force will be the sum of the Lagrange multipliers obtained in the analysis. From a physical point of view we expect that for an increasing value of the gravity we will have an increasing value of the global contact force as well, whose value will depend smoothly on the gravity.

In Fig. 4.6c-d the capacity of the two numerical techniques to reproduce this phenomenon has been studied. On the left the global contact force is plotted in function of the gravity, while on the right the error respect to a reference solution obtained with a very fine mesh ($h = 0.04$) is plotted. In particular we can observe that the standard LME curve presents two significant discontinuities. This is due to the fact that when the gravity is increased a larger part of the domain enters in contact with the rigid surface. However, since with LME approximants the boundary is represented by the polygonal mesh used for the integration, a discontinuity occurs when a different number of nodes reaches the contact with the surface. On the contrary, we notice that the IGA-LME approach allows us to have a smoother reproduction of the phenomenon. Moreover the better representation of the boundary allows to reduce the error.

4.4.4 Contact of a complex-shaped indenter

To assess the findings of the previous section a second application where the boundary of the domain is defined by a given complex-shaped B-spline curve was considered. The cloud of nodes (external ring of control points + internal

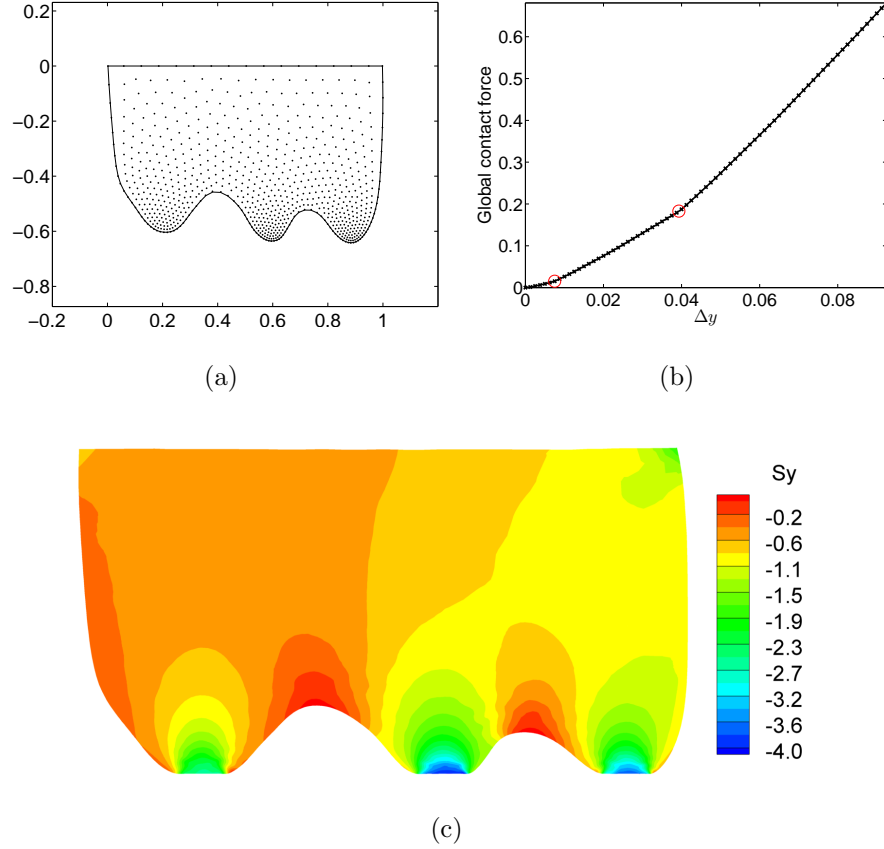


Figure 4.7: Contact of a complex-shaped indenter with a rigid surface; (a) the domain and the cloud of nodes used for the analysis; (b) the global contact force in function of the imposed displacement Δy . In the graph we assume $\Delta y = 0$ when the contact starts. Note that the slope changes in three different zones because the stiffness depends on how many parts of the domain enters in contact with the rigid surface; (c) the σ_y stress for $\Delta y = 0.1$.

nodes) used for the simulation is represented in Fig. 4.7a. Again the isogeometric parametrization was employed only on the inferior patch of the domain while in the top standard LME interpolants was used. In this problem the indenter was forced to enter in contact with a rigid surface imposing a fixed displacement to the above segment.

The density of nodes was increased in the bottom of the domain in order

4.4 Simulation of contact problems

to better reproduce the contact. The mesh generation was realized using the *distmesh* code for Matlab (120).

In Fig. 4.7b we can observe a plot of the global contact force in function of the displacement. Also for this application a smooth dependence is obtained. In Fig. 4.7c a map of the vertical stress σ_y for an advancement $\Delta y = 0.1$ is plotted.

5

Simulation of forming processes with max-ent approximants

5.1 Introduction

Once meshless methods acquired an important maturity several applications arose in the simulations of metal forming processes. Although in some studies the strong form of the problem was directly treated with collocation techniques (55, 56, 57), in the majority of the literature a Galerkin approximation based on the weak form was preferred. In fact the applicability of collocation formulations to metal forming is limited by aspects such as the description occurring in the vicinity of the boundary of the domain, or contact and friction implementation (58).

In the Galerkin framework the first reference works are due to Chen(59, 60) that applied the RKPM together with elasto-plastic material models. In (61) the SCNI scheme was also introduced to improve the rapidity of the method. Some examples of bulk metal forming are shown in these papers.

Then the majority of the literature is due to Cueto and Alfaro that employed the NEM approximants and assumed a viscoplastic behaviour of the material. In fact, according to chapter 2, it is an accepted assumption to neglect elastic deformations and therefore treat the material as a non-newtonian viscoplastic fluid, in the so called *flow formulation*. This aspect is discussed in detail in

(4). Other works on the application of the NEM to the simulation of extrusion are (28, 62, 63, 64, 65). In the latter reference numerical aspects related to computational cost and accuracy were deeply studied. In particular, Natural Element and Finite Element methods were compared and it was found that the computational cost of NEM was higher, especially if Sibson shape functions are used. However, as mentioned before, this problem is negligible for highly nonlinear applications. Besides the simulation of extrusion the NEM has been employed also in many other applications and produced appealing results for many forming processes like friction stir welding (66), forging (67), casting (63), laser surface coating (68), machining (69), and many others.

The application of meshless formulations to this type of processes is not straightforward due to the issues related to the imposition of incompressibility. In fact, in the simulation of incompressible flows, even if meshless methods are less sensible than FEM to volumetric locking it is still preferable to employ mixed pressure-velocity formulations. This poses some issues regarding the construction of a discretization that satisfies the *inf-sup* or LBB compatibility condition (121, 122). While in the FEM environment different type of shape functions, defined on the same elements, can be used for the velocity and the pressure the problem becomes more complicated for meshless methods. In the works based on the Natural Element Method the NN approximants are used for the velocities and constant approximants directly defined on the Voronoi diagram are used for the pressure. However, even if the method performs well, some oscillations are still present.

As an original contribution of this project a stabilized mixed formulation based on LME approximants is proposed. Since the same basis functions approximate the velocity and the pressure a stabilization approach is employed to circumvent the LBB condition. As it was already mentioned in chapters 2 and ??, a good approximation for metal forming problems is to treat the material as a non-newtonian incompressible viscoplastic fluid. Therefore, due to the analogy with the Stokes equations, a stabilization method proposed for fluid dynamics was extended to metal forming applications. Recently a family of consistent stabilization techniques has been widely studied in the literature (123, 124, 125). In particular, in this chapter, a modification of the technique used in (125), that is

5.2 The stabilized viscoplastic formulation

equivalent to the penalization of the incompressibility equation with the gradient of the pressure is proposed. This approach recovers a strategy already proposed in (126). In the following the resulting formulation is presented together with some implementation details and then some reference metal forming and orthogonal cutting problems are studied.

5.2 The stabilized viscoplastic formulation

The governing equations for the *flow formulation* of viscoplasticity take the form:

$$\nabla \cdot \boldsymbol{\sigma} = \mathbf{f} \text{ in } \Omega \quad (5.1a)$$

$$\nabla \cdot \mathbf{v} = 0 \text{ in } \Omega \quad (5.1b)$$

$$\mathbf{v} = \mathbf{v}_d \text{ in } \Gamma_d \quad (5.1c)$$

where Ω is the computational domain, \mathbf{v} the velocity vector, \mathbf{v}_d the imposed velocity for the Dirichlet conditions in Γ_d , and \mathbf{f} the body force ; $\boldsymbol{\sigma}$ is the Cauchy stress tensor. In the *flow formulation* the elastic deformations are neglected and the stress tensor follows from

$$\boldsymbol{\sigma} = 2\mu\mathbf{d} - p\mathbf{I} \quad (5.2)$$

where \mathbf{d} is the rate-of-deformation and p is the pressure; μ is the viscosity that in the general case depends on \mathbf{d} and on the temperature T . Here, for simplicity, we assume isothermal conditions. Thus, once $\mu(\mathbf{d})$ is given the above equations provide a boundary value problem for \mathbf{v} and p . As far as the material behaviour is concerned in the numerical applications presented in this chapter a simplified Norton-Hoff power law has been adopted like in section 2.3:

$$S_f = Cd^n \quad (5.3)$$

where S_f is the flow stress and $d = \sqrt{\frac{2}{3}d_{ij}d_{ij}}$ is the equivalent strain rate. The viscosity then also depends on d with the relation:

$$\mu = \mu_0(\sqrt{3}d)^{n-1} \quad (5.4)$$

5.2 The stabilized viscoplastic formulation

where $C = 3\mu_0$.

The weak form of the equilibrium equation is:

$$\int_{\Omega} \nabla \boldsymbol{\sigma} : \delta \mathbf{d} \, d\Omega - \int_{\Omega} \mathbf{f} \cdot \delta \mathbf{v} \, d\Omega = 0 \quad (5.5a)$$

$$\int_{\Omega} \nabla \cdot \mathbf{v} \delta p \, d\Omega = 0 \quad (5.5b)$$

According to (124) the general way to stabilize the problem is to add to the aforementioned equations a consistent term in the form:

$$\delta \Pi_S = \int_{\Omega} \tau \mathcal{P}(\delta \mathbf{v}, \delta p) R(\mathbf{v}, p) \, d\Omega \quad (5.6)$$

where $R(\mathbf{v}, p)$ is the residual of the strong form of the problem (which ensures the consistency of the new weak form), τ is a parameter which controls the amount of stabilization and $\mathcal{P}(\delta \mathbf{v}, \delta p)$ is a partition of the differential operator. Choosing $\mathcal{P}(\delta \mathbf{v}, \delta p) = \nabla \delta p$ we recover the *simplified Galerkin Least Squares scheme* that was firstly proposed by Hughes (127) and it is also known as *pressure-Poisson stabilized Galerkin method* (125):

$$\delta \Pi_S = \int_{\Omega} \tau \nabla \delta p (\nabla \boldsymbol{\sigma} - \mathbf{f}) \, d\Omega = \int_{\Omega} \tau \nabla \delta p (\nabla \cdot (2\mu \mathbf{d}) - \nabla p - \mathbf{f}) \, d\Omega \quad (5.7)$$

As commonly done in finite element methods the second order term $\nabla \cdot (2\mu \mathbf{d})$ will be neglected in the new formulation. Indeed, for low order finite elements, the first part of the consistent term is zero. A stabilization approach that involves only the gradient of the pressure has been also independently proposed in (126). This simplification avoids the computation of the second derivatives of the basis functions, which can be cumbersome and ill-posed near the boundary (90, 107). Thus the stabilization is given only by:

$$\delta \Pi_S = \int_{\Omega} \tau \nabla \delta p (-\nabla p - \mathbf{f}) \, d\Omega \quad (5.8)$$

This formulation is still numerically consistent, by making the parameter τ dependent on the nodal spacing as

$$\tau = \frac{C_s}{\mu} \bar{\rho}^2 \quad (5.9)$$

5.2 The stabilized viscoplastic formulation

For regular meshes $\bar{\rho}$ is equal to the nodal spacing h , while for irregular meshes excellent results were found by calculating $\bar{\rho}$ as a simple average of the neighbours to a given integration point. The following algorithm was used:

- calculate the Delaunay triangulation of the cloud of nodes which is used for the integration
- for each node calculate the local mesh size h_i as a mean of the distance from its natural neighbours in the triangulation
- for each integration point calculate the max-ent shape functions using for the nodes $\beta_i = \gamma/h_i^2$
- for each integration point calculate $\bar{\rho}$ as a mean of h_i of its neighbours

Note that $\tau \rightarrow 0$ with the mesh refinement and, therefore, the numerical method is consistent. This aspect is further discussed in (125, 128).

The choice of C_s is in general problem dependent. For the finite elements this topic has been analyzed in (129) and is also discussed in (123). In general, when C_s is increased, the quality of the results in terms of regularity of the solutions is improved but the accuracy is worsened due to the error in the penalization. In the numerical applications studied in this project very good results were achieved with C_s in the range from 0.5 to 2. In particular a value of $C_s = 0.5$ was set in all the applications shown in the following.

Finally the weak form of the problem has to be completed with a contribution associated to the Dirichlet and the contact conditions on the boundary. As mentioned before the LME basis function posses the Kronecker-delta property on all the convex part of the domain, so the imposition of the essential condition has to be included in the weak form only if it is required in some non-convex part of the domain. Using a Lagrange multipliers approach the following term has to be added to the energy:

$$\delta\Pi_D = \int_{\Omega} \boldsymbol{\lambda} \cdot (\mathbf{v} - \mathbf{v}_d) d\Gamma \quad (5.10)$$

In the case of contact (118), according to section 4.4.1, a gap function g_n is defined for any point on the work-piece (slave surface) and the constraint $g_n \geq 0$ is imposed. From a mathematical point of view the strong form of the problem is

5.2 The stabilized viscoplastic formulation

modified with the Signorini condition (118) that for sake of clarity was omitted in eq. 5.1. However, from the implementation point of view, the contact conditions are imposed by adding to the weak form a contribution known as contact energy. On using a Lagrange multipliers approach the following energy is added:

$$\delta\Pi_C = \int_{\Gamma_c} \lambda g_n d\Gamma \quad (5.11)$$

this term enforces the condition $g_n = 0$; thus an iterative approach is required to determine the correct region of the workpiece that enters in contact with the tool. Since also the non-linear character of the governing equations requires an iterative resolution, this task is normally carried in coupling with the resolution.

It is worth to note that in most of the practical applications (see Section 5.3) the domain become non convex in those zones where the contact with the tool is imposed. The lack of the Kronecker-delta property, that the max-ent interpolants exhibit in the non-convex part of the domain, requires a Lagrange multipliers approach to impose the Dirichlet conditions in the boundary of such parts, while in other techniques like FEM or NEM the conditions can be directly imposed on the nodes. However, when contact conditions are introduced, a Lagrange multipliers approach is anyway required also for the methods that are interpolant on the boundary. For this reasons, although some modifications of the max-ent formulation that gives interpolant functions also in the non-convex parts of the domain are possible (17, 83), the lack of this property does not have a big influence on the performance of the method.

Once the weak form of the problem is obtained it is discretized in space and in time. The latter task is performed using an updated Lagrangian approach. The displacement is updated from a given displacement $\mathbf{u}(t)$ and the calculated velocity $\mathbf{v}(t + \Delta t)$ in the following way:

$$\mathbf{u}(t + \Delta t) = \mathbf{u}(t) + \mathbf{v}(t + \Delta t) \Delta t \quad (5.12)$$

The velocity and the pressure are discretized likewise. Using the FEM standard notation, we define:

$$\mathbf{N} = \begin{pmatrix} \varphi_1 & 0 & \dots & 0 \\ 0 & \varphi_1 & \dots & \varphi_N \end{pmatrix}, \quad \boldsymbol{\varphi} = (\varphi_1, x \dots \varphi_N) \quad (5.13)$$

5.2 The stabilized viscoplastic formulation

and

$$\mathbf{B} = \begin{pmatrix} \varphi_{1,x} & 0 & \dots & 0 \\ 0 & \varphi_{1,y} & \dots & \varphi_{N,y} \\ \varphi_{1,y} & \varphi_{1,x} & \dots & \varphi_{N,x} \end{pmatrix} \quad (5.14)$$

the approximated weak form of the problem, in matricial form, will be:

$$\begin{bmatrix} \mathbf{K} & \mathbf{G} & \mathbf{L} \\ \mathbf{G}^T & \mathbf{M}_S & \mathbf{0} \\ \mathbf{L}^T & \mathbf{0} & \mathbf{0} \end{bmatrix} \begin{bmatrix} \mathbf{V} \\ \mathbf{P} \\ \mathbf{\Lambda} \end{bmatrix} = \begin{bmatrix} \mathbf{F} \\ \mathbf{F}_S \\ \mathbf{0} \end{bmatrix} \quad (5.15)$$

where

$$\mathbf{K} = \int_{\Omega} \mathbf{B}^T \boldsymbol{\mu} \mathbf{B} \, d\Omega, \quad \boldsymbol{\mu} = \begin{pmatrix} 2\mu & 0 & 0 \\ 0 & 2\mu & 0 \\ 0 & 0 & \mu \end{pmatrix}, \quad \mathbf{F} = \int_{\Omega} \mathbf{N}^T \mathbf{f} \, d\Omega \quad (5.16)$$

$$\mathbf{G} = \int_{\Omega} -\mathbf{B}^T \mathbf{1} \varphi \, d\Omega, \quad \mathbf{1} = \begin{pmatrix} 1 \\ 1 \\ 0 \end{pmatrix} \quad (5.17)$$

$$\mathbf{M}_S = \int_{\Omega} -\tau (\nabla \varphi)^T \nabla \varphi \, d\Omega, \quad \mathbf{F}_S = \int_{\Omega} \tau (\nabla \varphi)^T \mathbf{f} \, d\Omega \quad (5.18)$$

Observing that the viscosity μ depends on the equivalent strain rate d , that is a function of the derivatives of the velocity, a non-linearity is present in the matrix \mathbf{K} . As mentioned for the nodal integrated FEM the most used methods to treat this non-linearity are the Newton-Raphson scheme and the Direct Iteration Method (1).

In the first case a system analogous to eq. 5.15 is iteratively solved but the matrix $\boldsymbol{\mu}$ is substituted with the material tangent matrix and the right hand side contains also the residuals of the weak form (4). The problem of such a scheme is that when highly non-linear problems are studied the method does not converge unless an initial solution close enough to the final one is used.

The Direct Iteration Method starts assuming the viscosity constant and given by the value from the previous instant. Then the velocity is obtained and the viscosity is recalculated. The new values of the viscosity give a new velocity field and so on the method is iterated until convergence. Even if a slightly higher number of iterations is required this approach is more robust than the Newton scheme. Anyway the best strategy is in fact to combine the two schemes, using

the Direct Iteration Method to find an initial solution and then refining it with the Newton Raphson method.

Concerning the numerical integration it was performed using the Delaunay triangulation of the cloud of nodes in combination with the alpha-shape technique (31). The Delaunay algorithm is the easiest way to obtain a triangulation for a given cloud of nodes but such triangulation is extended to the whole convex hull of the cloud. Therefore using the alpha-shape criterion the mesh has to be modified removing the triangles whose circum-radius is bigger than a given value. This approach has been already successfully applied in other reference works such (63), where its application is discussed in detail.

5.3 Numerical examples

In this section the validity of the stabilized viscoplastic formulation is confirmed some numerical results in the simulation of reference manufacturing processes. Since the scope of this project was only to investigate on the potentialities of the new technique some simplifications were introduced in the modelling of the problems, such as neglecting friction and thermal phenomenon. As far as the material behaviour is concerned the coefficients for the Norton-Hoff power were $\mu_0 = 150$ and $n = 0.2$. According to (30) these values are typical of some aluminium alloys.

In all the examples the LME basis functions were constructed with a value of $\gamma = 1.6$.

5.3.1 Upsetting

The first application that was considered is the upsetting of a cylindrical billet that is progressively flattened between two plates. The domain represented in fig. 5.1 has been discretized with 524 nodes and 100 time steps ($\Delta t = 1$) has been considered.

This process is a very good benchmark to test the efficiency of the stabilization because due to the regularity of the domain a likewise trend of the variables is

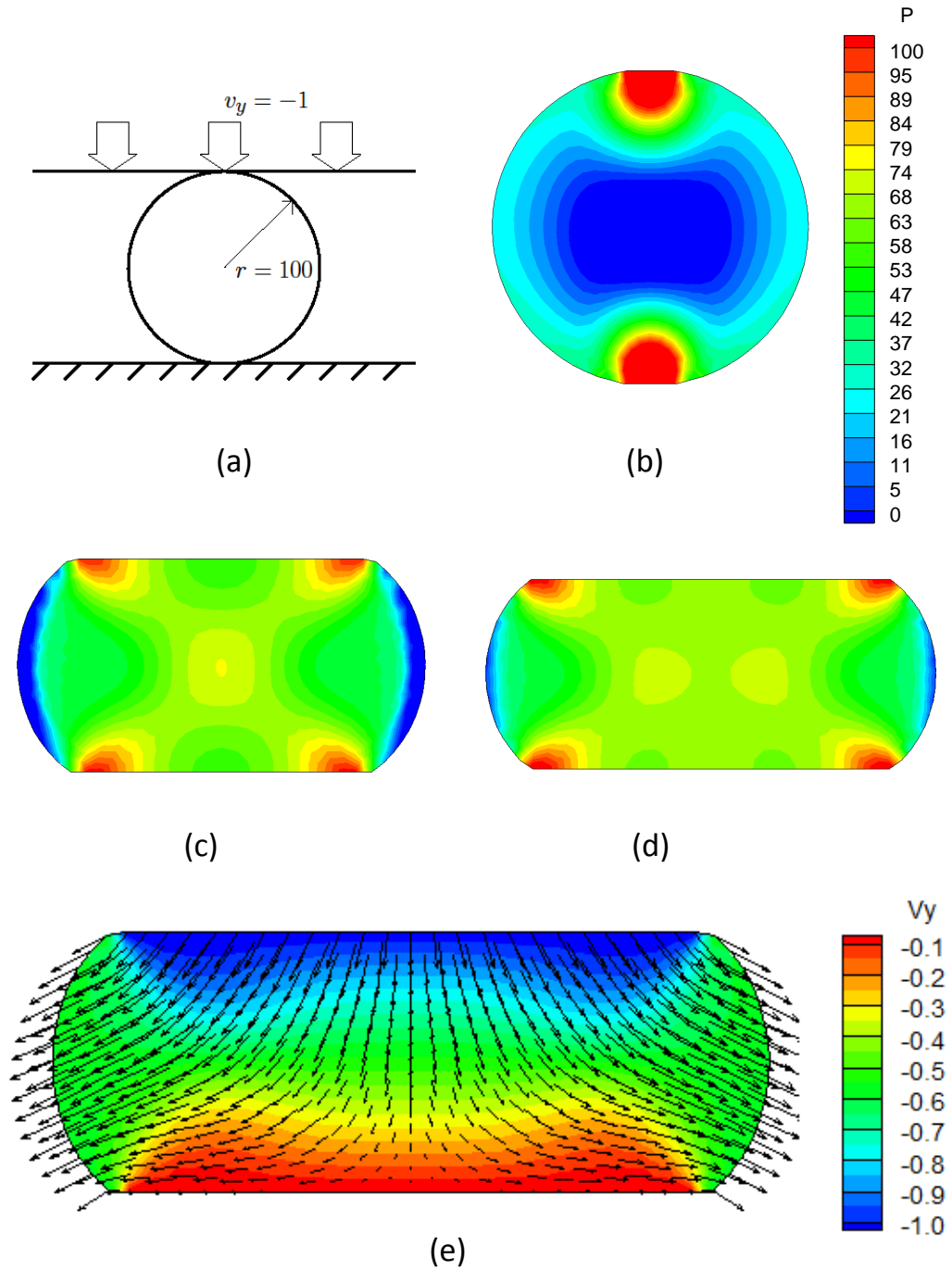


Figure 5.1: Upsetting; (a) sketch of the geometry; (b-d) pressure at different time steps; (e) vertical velocity at the end of the process.

expected and eventual oscillations can be easily detached. According to fig. 5.1 the method performs very well and perfectly smoothed maps are obtained for both the velocity and the pressure field.

5.3.2 Extrusion

Extrusion is a typical forming process where the application of the finite element method is stressed by the heavy mesh distortions. For this reason and for the importance of its simulation in the industrial applications this process has been widely studied in the literature on the meshless methods for metal forming.

In this example a simple model were considered (fig. 5.2). The initial domain was discretized with a 32×32 grid of nodes; 100 time steps ($\Delta t = 0.3$) were considered. The shape of the profile during the process was determined only by the means of the alpha-shape criterion. Despite the simplicity of this approach we can note that also in this case very high quality maps are obtained for both the velocity and the pressure field, even in the zones where high deformations are present.

It is also interesting to observe a comparison between the trend of the pressure field predicted with the LME approximants in this application and the pressure field predicted with the NI-FEM in the problem studied in section 2.3. In figure 5.3 we can observe a significant improvement in the regularity of the field. Although the two problems studied are slightly different it is evident that the LME approximants outperform the NI-FEM in the quality of the approximation.

To assess the accuracy of the max-ent solution the process was also simulated with the commercial FEM code DEFORMTM. In fig. 5.4 a comparison was made between the prediction of the pressure trend with the two codes along the x and the y axes (see fig. 5.2a) at the first step of the simulation. A good agreement between the curves can be observed on the symmetry axis (x) and they are expected to match with mesh refinement. The two codes give the same prediction also along the y axes in the first part of the bottom of the die and in the zone where the material is free to flow but the commercial code provides a higher prediction of the pressure peak. In this case the smoothness of the max-ent basis functions does not allow to reproduce such a sharp trend with only a

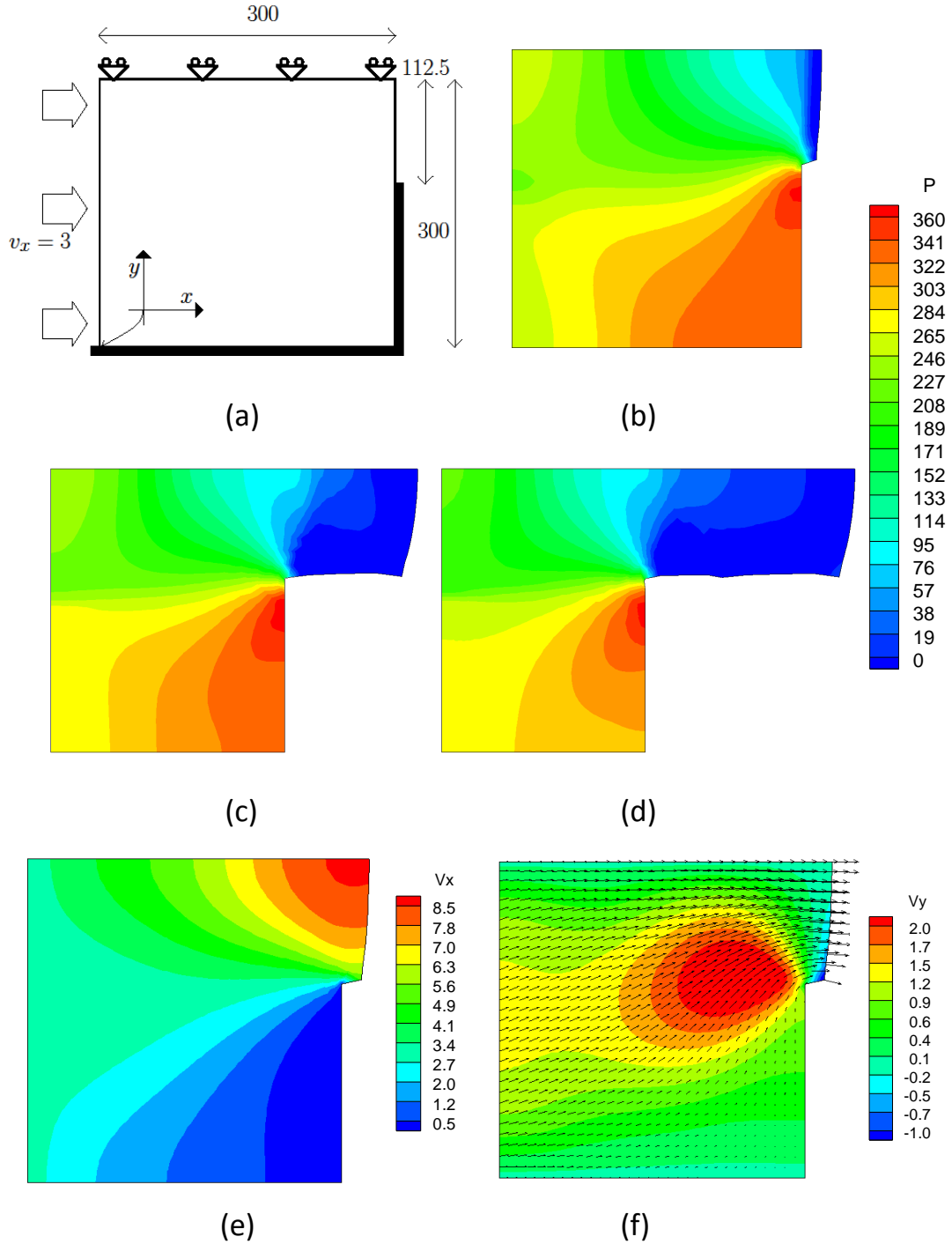


Figure 5.2: Extrusion; (a) sketch of the geometry; (b-d) pressure at different time steps; (e) horizontal velocity at the tenth step; (f) vertical velocity at the tenth step.

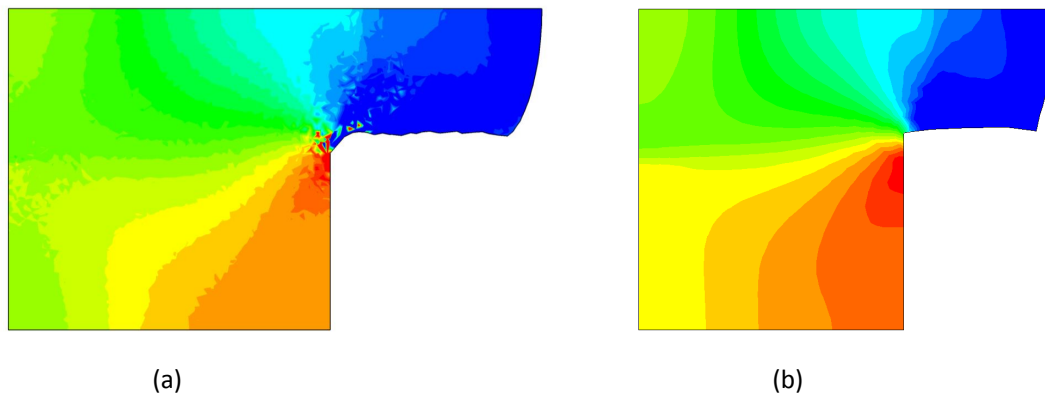


Figure 5.3: A comparison between the NI-FEM (a) and LME (b) predictions of pressure fields. Note that the two problems are different.

reduced number of nodes. However, the simplified model that has been used for both simulations assumes a rigid and perfectly straight die (fig. 5.2a) while in the reality the dies have some curvature as well as the trend of the pressure field is more regular. This consideration is confirmed observing that, if the DEFORMTM die is smoothed with a curvature of a given radius r , the peak progressively decreases when r is increased.

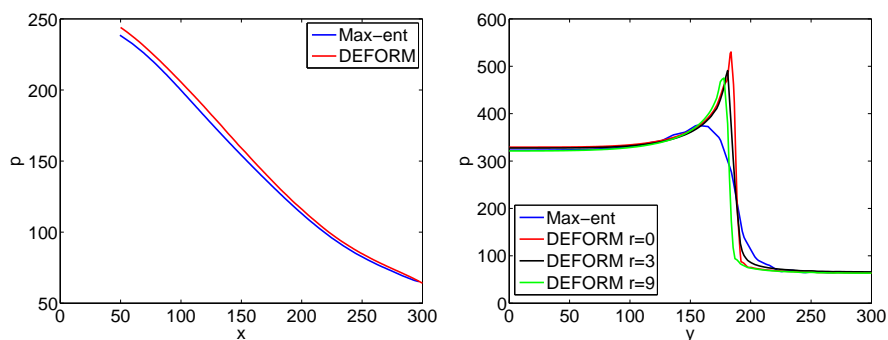


Figure 5.4: Pressure along the symmetry axis x for $y = 300$ (left) and on the bottom of the die along the y axis for $x = 300$ (right) at the beginning of the simulation. A comparison between the max-ent and the DEFORM predictions.

5.3.3 Orthogonal cutting

The simulation of machining processes is another application where the mesh is heavily distorted during the analysis; therefore the use of meshfree approximants is a possible alternative to the FEM that is worth to be investigated also in this field. However, while in metal forming several applications are available in the literature, nothing has been done yet, to the author of this work's knowledge, in the simulation of cutting or others machining processes. Here a simple model of orthogonal cutting (fig. 5.5) was considered. The domain was discretized using a 5000 nodes mesh with a node spacing $h \approx 0.33$ in the cutting zone. The simulation was subdivided in 350 time steps with an increment $\Delta t = 2 \cdot 10^{-5}$. As we can see in fig. 5.5(b-f) also in this application a regular trend for the pressure is obtained and the method performs well in the prediction of the pressure pick close to the tool tip. The results however are worsened at the end of the simulation (fig. 5.5 (f)) because although the method is not sensible to the distortions of the mesh (that is used only for the integration) their quality is anyway affected by the regularity of the node distribution. As we can note fig. 5.5 (g) the mesh that was originally regular becomes heavily distorted and, in addition, the density of the nodes is no more regular in some zones. Even if the method performs well for such a distorted mesh (this would not be the case of finite elements) a rezoning would be beneficial to continue the simulation. In fact, this operation is not significantly time consuming when meshfree approximants are used.

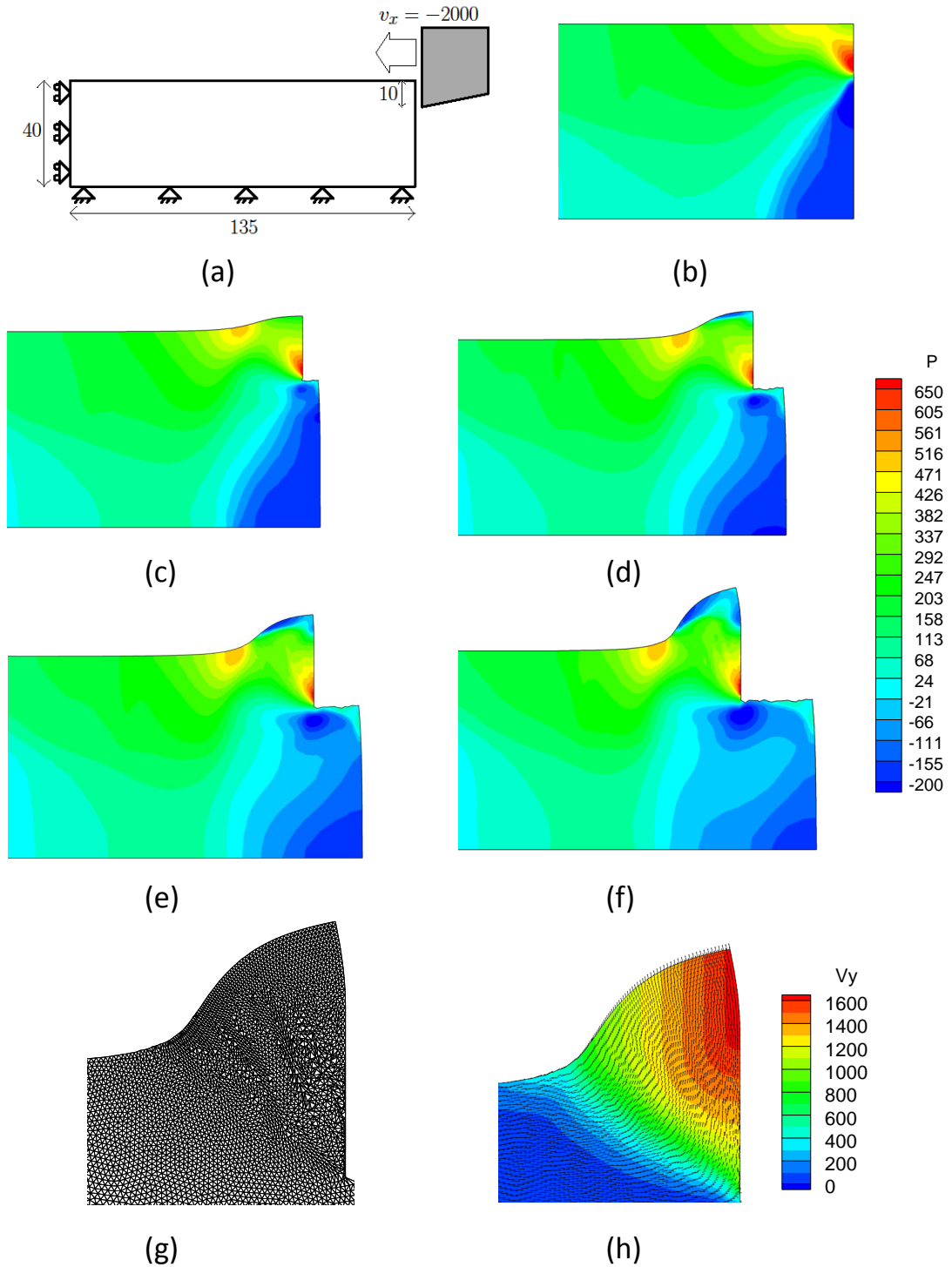


Figure 5.5: Orthogonal cutting; (a) sketch of the geometry; (b-f) pressure at different time steps; (g) mesh at the 350th step; (h) vertical velocity at the 350th step.

6

Concluding remarks

In this work two numerical techniques recently proposed as an alternative to the classical FEM has been analysed and applied to the simulation of benchmark problems in metal forming and orthogonal cutting. Some original developments has been provided to both techniques as well.

The biggest drawback of the traditional FEM formulation is that the quality of the results deeply depends on the characteristic of the mesh and therefore the large deformations involved in forming processes require remeshing-rezoning techniques that affect the computational times and the flexibility of the analysis. In this framework, the Nodal Integrated Finite Element Method is a valid alternative since it performs well also with very distorted meshes. Different nodal integration schemes have been studied and applied to metal forming simulation in this work. Also the stabilization of the spurious low energy modes, a recurrent problem in the nodal integration context, has been taken into account. The results provided in the numerical examples confirmed the validity of the method particularly in the applications where the standard FEM formulation is forced to deal with high mesh distortions. As drawback, the nodal averaging of the strain gives some numerical irregularities in the pressure fields which do not have a physical matching.

In the family of meshless methods the *Maximum Entropy* approximants, despite their recent introduction, have shown a lot of potentialities in several applications. In this work, as an original contribution to the numerical development of the method, the problem of the computation of the derivatives of the

basis functions on the boundary of the domain has been solved. Furthermore the blending with Iso-geometric functions has been studied in the simulation of small deformation contact problems in linear elasticity. Finally the application of such approximants has been extended also to material forming. In doing so the problem of the construction of an LBB compliant approximation has been circumvented by means of consistent stabilization techniques already proposed in fluid dynamics. The numerical results in both bulk metal forming and manufacturing applications assessed the validity of the formulation and showed very high quality results. Thanks to the smoothness of the max-ent basis functions a better regularity of the variables approximation has been observed respect to the nodal integrated FEM. In addition, the physical consistency of the model is preserved. This is not the case of the NI-FEM where the numerical fluctuations affect the regularity of the stress fields. The results found in this work are a very encouraging starting point to further develop the method and to extend it to more applications. In particular the generalization of the isogeometric formulation to large deformation contact problems would be suitable for the simulation of all the material forming processes. The extension to three-dimensional applications and the introduction of more elaborated material models would be an important development as well.

References

- [1] SHIRO KOBAYASHI, SOO IK OH, AND TAYLAN ALTAN. *Metal forming and the finite-element method*. Oxford University Press, 1989. 1, 12, 54
- [2] D. PERIC AND D. R. J. OWEN. *Computational Modeling of Forming Processes*. John Wiley & Sons, Ltd, 2004. 1
- [3] I. BABUSKA AND A. K. AZIZ. **On the Angle Condition in the Finite Element Method**. *SIAM Journal on Numerical Analysis*, **13**(2):pp. 214–226, 1976. 1
- [4] I. ALFARO, D. GONZLEZ, D. BEL, E. CUETO, M. DOBLARÉ, AND F. CHINESTA. **Recent advances in the meshless simulation of aluminium extrusion and other related forming processes**. *Archives of Computational Methods in Engineering*, **13**(1):3–43, 2006. 1, 49, 54
- [5] O. C. ZIENKIEWICZ AND P. N. GODBOLE. **Flow of plastic and visco-plastic solids with special reference to extrusion and forming processes**. *International Journal for Numerical Methods in Engineering*, **8**(1):1–16, 1974. 1, 10
- [6] ZIENKIEWICZ O.C. *Flow formulation for numerical solution of forming processes*. John Wiley, Chichester, 1984. 1, 10
- [7] Y. J. HWU AND J. G. LENARD. **A finite element study of flat rolling**. *Journal of Engineering Materials and Technology*, **110**(1):22 – 27, 1988. 1
- [8] JOHN T. CARROLL III AND JOHN S. STRENKOWSKI. **Finite element models of orthogonal cutting with application to single point diamond turning**. *International Journal of Mechanical Sciences*, **30**(12):899 – 920, 1988. 1
- [9] T. BELYTSCHKO AND J. M. KENNEDY. **Computer models for subassembly simulation**. *Nuclear Engineering and Design*, **49**:17–38, 1978. 2
- [10] WING KAM LIU, CHANG HERMAN, CHEN JUUN-SHYAN, AND BELYTSCHKO TED. **Arbitrary lagrangian-eulerian petrov-galerkin finite elements for nonlinear continua**. *Computer Methods in Applied Mechanics and Engineering*, **68**(3):259 – 310, 1988. 2
- [11] YU-KAN HU AND WING KAM LIU. **An ALE hydrodynamic lubrication finite element method with application to strip rolling**. *International Journal for Numerical Methods in Engineering*, **36**(5):855–880, 1993. 2
- [12] R. RAKOTOMALALA, P. JOYOT, AND M. TOURATIER. **Arbitrary Lagrangian-Eulerian thermomechanical finite-element model of material cutting**. *Communications in Numerical Methods in Engineering*, **9**(12):975–987, 1993. 2
- [13] LARS OLOVSSON, LARSGUNNAR NILSSON, AND KJELL SIMONSSON. **An {ALE} formulation for the solution of two-dimensional metal cutting problems**. *Computers Structures*, **72**(45):497 – 507, 1999. 2
- [14] T. BELYTSCHKO, Y. KRONGAUZ, D. ORGAN, M. FLEMING, AND P. KRYSL. **Meshless methods: An overview and recent developments**. *Computer Methods in Applied Mechanics and Engineering*, **139**:3–47, 1996. 2, 23
- [15] C.R. DOHRMANN, M. W. HEINSTEIN, J. JUNG, S. W. KEY, AND W. R. WITKOWSKI. **Node-based uniform strain elements for three-node triangular and four-node tetrahedral meshes**. *International Journal for Numerical Methods in Engineering*, **47**(9):1549–1568, 2000. 2, 5, 7, 8
- [16] M. ARROYO AND M. ORTIZ. **Local maximum-entropy approximation schemes: a seamless bridge between finite elements and meshfree methods**. *International Journal for Numerical Methods in Engineering*, **65**(13):2167–2202, 2006. 2, 25, 27, 29, 33, 39
- [17] A. ROSOLEN AND M. ARROYO. **Blending isogeometric analysis and maximum entropy meshfree approximants**. 2012. In preparation. 3, 33, 34, 36, 37, 45, 53
- [18] M. A. PUSO AND J. SOLBERG. **A stabilized nodally integrated tetrahedral**. *International Journal for Numerical Methods in Engineering*, **67**(6):841–867, 2006. 5, 10, 13
- [19] STEPHEN BEISSEL AND TED BELYTSCHKO. **Nodal integration of the element-free Galerkin method**. *Computer Methods in Applied Mechanics and Engineering*, **139**(14):49 – 74, 1996. 5

REFERENCES

- [20] JIUN-SHYAN CHEN, CHENG-TANG WU, SANGPIL YOON, AND YANG YOU. **A stabilized conforming nodal integration for Galerkin mesh-free methods.** *International Journal for Numerical Methods in Engineering*, **50**(2):435–466, 2001. 5, 7, 24, 25
- [21] JIUN-SHYAN CHEN, SANGPIL YOON, AND CHENG-TANG WU. **Non-linear version of stabilized conforming nodal integration for Galerkin mesh-free methods.** *International Journal for Numerical Methods in Engineering*, **53**(12):2587–2615, 2002. 5
- [22] M. A. PUSO, J. S. CHEN, E. ZYWICZ, AND W. ELMER. **Mesh-free and finite element nodal integration methods.** *International Journal for Numerical Methods in Engineering*, **74**(3):416–446, 2008. 5
- [23] F.P. PREPARATA AND MI SHAMOS. *Computational Geometry: An introduction.* Springer, New York, 1985. 7, 23
- [24] J.B. LASSERRE. **An analytical expression and an algorithm for the volume of a convex polyhedron in \mathbf{R}^n .** *Journal of Optimization Theory and Applications*, **39**(3):363–377, 1983. 9
- [25] J.L. CHENOT AND M. BELLET. **The Viscoplastic Approach for the Finite-Element Modelling of Metal-Forming Processes.** In PETER HARTLEY, IAN PILLINGER, AND CLIVE STURGESS, editors, *Numerical Modelling of Material Deformation Processes*, pages 179–224. Springer London, 1992. 10
- [26] C. M. SELLARS AND W.J.M. TEGART. **Hot workability.** *International Metallurgical Review*, 1972. 11
- [27] J LOF AND Y BLOKHUIS. **{FEM} simulations of the extrusion of complex thin-walled aluminium sections.** *Journal of Materials Processing Technology*, **122**(23):344 – 354, 2002. 11
- [28] I. ALFARO, F. GAGLIARDI, J. OLIVERA, E. CUETO, L. FILICE, AND F. CHINESTA. **Simulation of the extrusion of hollow profiles by Natural Element Methods.** *International Journal of Material Forming*, **2**(SUPPL. 1):597–600, 2009. 11, 49
- [29] *Creep of steel at high temperatures.* McGraw-Hill Book Co., New York., 1929. 11
- [30] S. KALPAKJIAN. *Manufacturing Processes for Engineering Materials, 5/e (New Edition).* Pearson Education, 1992. 11, 20, 55
- [31] H. EDELSBRUNNER, D. KIRKPATRICK, AND R. SEIDEL. **On the shape of a set of points in the plane.** *Information Theory, IEEE Transactions on*, **29**(4):551–559, 1983. 13, 33, 55
- [32] R. A. GINGOLD AND J. J. MONAGHAN. **Smoothed particle hydrodynamics - Theory and application to non-spherical stars.** *Mon. Not. Roy. Astron. Soc.*, **181**:375–389, November 1977. 22
- [33] WING KAM LIU, SUKKY JUN, AND YI FEI ZHANG. **Reproducing kernel particle methods.** *International Journal for Numerical Methods in Fluids*, **20**(8-9):1081–1106, 1995. 22
- [34] WING KAM LIU, SUKKY JUN, SHAOFAN LI, JONATHAN ADEE, AND TED BELYTSCHKO. **Reproducing kernel particle methods for structural dynamics.** *International Journal for Numerical Methods in Engineering*, **38**(10):1655–1679, 1995. 22
- [35] B. NAYROLES, G. TOUZOT, AND P. VILLON. **Generalizing the finite element method: Diffuse approximation and diffuse elements.** *Computational Mechanics*, **10**(5):307–318, 1992. 22
- [36] T. BELYTSCHKO, Y. Y. LU, AND L. GU. **Element-free Galerkin methods.** *International Journal for Numerical Methods in Engineering*, **37**(2):229–256, 1994. 23
- [37] T BELYTSCHKO, L GU, AND Y Y LU. **Fracture and crack growth by element free Galerkin methods.** *Modelling and Simulation in Materials Science and Engineering*, **2**(3A):519, 1994. 23
- [38] C.ARMANDO DUARTE AND J.TINSLEY ODEN. **An h-p adaptive method using clouds.** *Computer Methods in Applied Mechanics and Engineering*, **139**(14):237 – 262, 1996. 23
- [39] I. BABUSKA AND J.M. MELENK. **The Partition of Unity Method.** *International Journal of Numerical Methods in Engineering*, **40**:727–758, 1996. 23
- [40] J. M. MELENK AND I. BABUKA. **The partition of unity finite element method: Basic theory and applications.** *Computer Methods in Applied Mechanics and Engineering*, **139**:289–314, 1996. 23
- [41] N. SUKUMAR, B. MORAN, AND T. BELYTSCHKO. **The natural element method in solid mechanics.** *International Journal for Numerical Methods in Engineering*, **43**(5):839–887, 1998. 23
- [42] N. SUKUMAR AND B. MORAN. **C1 natural neighbor interpolant for partial differential equations.** *Numerical Methods for Partial Differential Equations*, **15**(4):417–447, 1999. 23
- [43] N. SUKUMAR, B. MORAN, A. YU SEMENOV, AND V. V. BELIKOV. **Natural neighbour Galerkin methods.** *International Journal for Numerical Methods in Engineering*, **50**(1):1–27, 2001. 23

REFERENCES

- [44] R. SIBSON. *A Brief Description of Natural Neighbour Interpolation*, **21**, pages 21–36. John Wiley & Sons, 1981. 23, 24
- [45] VITALI V. BELIKOV AND ANDREI YU. SEMENOV. **Non-Sibsonian interpolation on arbitrary system of points in Euclidean space and adaptive isolines generation**. *Applied Numerical Mathematics*, **32**(4):371 – 387, 2000. 23
- [46] E. CUETO, N. SUKUMAR, B. CALVO, M.A. MARTNEZ, J. CE-GOINO, AND M. DOBLAR. **Overview and recent advances in natural neighbour galerkin methods**. *Archives of Computational Methods in Engineering*, **10**(4):307–384, 2003. 23
- [47] FRANK C. GNTHNER AND WING KAM LIU. **Implementation of boundary conditions for meshless methods**. *Computer Methods in Applied Mechanics and Engineering*, **163**(14):205 – 230, 1998. 24
- [48] S. FERNÁNDEZ-MÉNDEZ AND A. HUERTA. **Imposing essential boundary conditions in mesh-free methods**. *Computer Methods in Applied Mechanics and Engineering*, **193**(12–14):1257–1275, 2004. 24
- [49] A. HUERTA AND S. FERNÁNDEZ-MÉNDEZ. **Enrichment and Coupling of the Finite Element and Meshless Methods**. *International Journal for Numerical Methods in Engineering*, **48**:1615–1636, 2000. 24
- [50] L. GAVETE, J. J. BENITO, S. FALCO, AND A. RUIZ. **Implementation of essential boundary conditions in a meshless method**. *Communications in Numerical Methods in Engineering*, **16**(6):409–421, 2000. 24
- [51] E. CUETO, M. DOBLAR, AND L. GRACIA. **Imposing essential boundary conditions in the natural element method by means of density-scaled δ -shapes**. *International Journal for Numerical Methods in Engineering*, **49**(4):519–546, 2000. 24
- [52] FRANCISCO CHINESTA, SERGE CESCOTTO, ELAS CUETO, AND PHILIPPE LORONG. *Natural Element Method for the Simulation of Structures and Processes*. John Wiley Sons, Inc., 2013. 24
- [53] S. N. ATLURI AND TULONG ZHU. **New concepts in meshless methods**. *International Journal for Numerical Methods in Engineering*, **47**(1-3):537–556, 2000. 24
- [54] SUVRANU DE AND KLAUS-JRGEN BATHE. **The method of finite spheres with improved numerical integration**. *Computers Structures*, **79**(2225):2183 – 2196, 2001. 24
- [55] J. BONET AND S. KULASEGARAM. **Correction and stabilization of smooth particle hydrodynamics methods with applications in metal forming simulations**. *International Journal for Numerical Methods in Engineering*, **47**(6):1189–1214, 2000. 48
- [56] Y.-M. GUO AND K. NAKANISHI. **A backward extrusion analysis by the rigidplastic integrallessmeshless method**. *Journal of Materials Processing Technology*, **140**(13):19 – 24, 2003. `je:titel;Proceedings of the 6th Asia Pacific Conference on materials Processing/ce:titel; 48`
- [57] HONGYU WEN, XIANGHUI DONG, CUNLIANG YAN, AND XUEYU RUAN. **Three dimension profile extrusion simulation using meshfree method**. *The International Journal of Advanced Manufacturing Technology*, **34**(3-4):270–276, 2007. 48
- [58] ELAS CUETO AND FRANCISCO CHINESTA. **Meshless methods for the simulation of material forming**. *International Journal of Material Forming*, pages 1–19, 2013. 48
- [59] J S CHEN, C PAN, C T WU, AND C ROQUE. **A Lagrangian reproducing kernel particle method for metal forming analysis**. *Comput. Mech.*, (21):289, 1998. 48
- [60] JIUN-SHYAN CHEN, CRISTINA MARIA OLIVEIRA LIMA ROQUE, CHUNHUI PAN, AND SRGIO TONINI BUTTON. **Analysis of metal forming process based on meshless method**. *Journal of Materials Processing Technology*, **8081**(0):642 – 646, 1998. 48
- [61] SANGPIL YOON AND JIUN-SHYAN CHEN. **Accelerated mesh-free method for metal forming simulation**. *Finite Elements in Analysis and Design*, **38**(10):937 – 948, 2002. `je:titel;2001 Robert J. Melosh Medal Competition/ce:titel; 48`
- [62] I. ALFARO, J. YVONNET, E. CUETO, F. CHINESTA, AND M. DOBLARÉ. **Meshless methods with application to metal forming**. *Computer Methods in Applied Mechanics and Engineering*, **195**(4849):6661 – 6675, 2006. 49
- [63] I. ALFARO, D. BEL, E. CUETO, M. DOBLARÉ, AND F. CHINESTA. **Three-dimensional simulation of aluminium extrusion by the δ -shape based natural element method**. *Computer Methods in Applied Mechanics and Engineering*, **195**(33-36):4269–4286, 2006. 49, 55
- [64] L. FILICE, I. ALFARO, F. GAGLIARDI, E. CUETO, F. MICARI, AND F. CHINESTA. **A preliminary comparison between finite element and meshless simulations of extrusion**. *Journal of Materials Processing Technology*, **209**(6):3039 – 3049, 2009. 49

- [65] I. ALFARO, J. YVONNET, F. CHINESTA, AND E. CUETO. **A study on the performance of natural neighbour-based Galerkin methods.** *International Journal for Numerical Methods in Engineering*, **71**(12):1436–1465, 2007. 49
- [66] I. ALFARO, G. RACINEUX, A. POITOU, E. CUETO, AND F. CHINESTA. **Numerical simulation of friction stir welding by natural element methods.** *International Journal of Material Forming*, **2**(4):225–234, 2009. 49
- [67] N. SUKUMAR, J. DOLBOW, A. DEVAN, J. YVONNET, FRANCISCO CHINESTA, D. RYCKELYNCK, P. LORONG, ICIAR ALFARO, MA MARTNEZ, E. CUETO, AND MANUEL DOBLAR. **Meshless Methods and Partition of Unity Finite Elements.** *International Journal of Forming Processes*, **8**:409–427, 2005. 49
- [68] DAVID GONZLES, DAVID BEL, E. CUETO, FRANCISCO CHINESTA, AND MANUEL DOBLAR. **Natural Neighbour Strategies for the Simulation of Laser Surface Coating Processes.** *International Journal of Forming Processes*, **10**:89–108, 2007. 49
- [69] FRANCISCO CHINESTA, PHILIPPE LORONG, DAVID RYCKELYNCK, MIGUEL ANGEL MARTINEZ, ELIAS CUETO, MANUEL DOBLAR, GRARD COFFIGNAL, MAURICE TOURATIER, AND JULIEN YVONNET. **Thermomechanical Cutting Model Discretisation. Eulerian or Lagrangian, Mesh or Meshless?** *International Journal of Forming Processes*, **7**:83–97, 2004. 49
- [70] N. SUKUMAR. **Construction of polygonal interpolants: a maximum entropy approach.** *International Journal for Numerical Methods in Engineering*, **61**(12):2159–2181, 2004. 25, 26, 29
- [71] N. SUKUMAR. **Maximum entropy approximation.** *AIP Conference Proceedings*, **803**(1):337–344, 2005. 25
- [72] M. ARROYO AND M. ORTIZ. *Meshfree Methods for Partial Differential Equations III*, **57** of *Lecture Notes in Computational Science and Engineering*, chapter Local Maximum-Entropy Approximation Schemes, pages 1–16. Springer, 2007. 25
- [73] THOMAS M. COVER AND JOY A. THOMAS. *Elements of Information Theory*. Wiley-Interscience, 99th edition, August 1991. 25, 26
- [74] R. T. ROCKAFELLAR. *Convex Analysis*. Princeton University Press, Princeton, NJ, 1970. 25
- [75] S. BOYD AND L. VANDENBERGHE. *Convex Optimization*. Cambridge University Press, Cambridge, UK, 2004. 25, 28
- [76] N. SUKUMAR AND R.W. WRIGHT. **Overview and construction of meshfree basis functions: From moving least squares to entropy approximants.** *International Journal for Numerical Methods in Engineering*, **70**(2):181–205, 2007. 25, 27, 28
- [77] C.J. CYRON, M. ARROYO, AND M. ORTIZ. **Smooth, second order, non-negative meshfree approximants selected by maximum entropy.** *International Journal for Numerical Methods in Engineering*, **79**(13):1605–1632, 2009. 25
- [78] D. GONZÁLEZ, E. CUETO, AND M. DOBLARÉ. **A higher-order method based on local maximum entropy approximation.** *International Journal for Numerical Methods in Engineering*, **83**(6):741–764, 2010. 25
- [79] A. ROSOLEN, D. MILLÁN, AND M. ARROYO. **Second order convex maximum entropy approximants with applications to high order PDE.** *International Journal for Numerical Methods in Engineering*, 2012. 25, 29
- [80] N. SUKUMAR AND R.J-B WETS. **Deriving the Continuity of Maximum-Entropy Basis Functions via Variational Analysis.** *SIAM Journal of Optimization*, **18**(3):914–925, 2007. 25
- [81] A BOMPADRE, B SCHMIDT, AND M ORTIZ. **Convergence Analysis of Meshfree Approximation Schemes.** *SIAM Journal on Numerical Analysis*, **Accepted**, 2012. 25
- [82] A BOMPADRE, L E PEROTTI, C CYRON, AND M ORTIZ. **Convergent meshfree approximation schemes of arbitrary order and smoothness.** *Computer Methods in Applied Mechanics and Engineering*, **221–222**:83–103, 2012. 25
- [83] K. HORMANN AND N. SUKUMAR. **Maximum entropy coordinates for arbitrary polytopes.** **27**, pages 1513–1520, 2008. *Proceedings of SGP 2008*. 25, 53
- [84] B. LI, F. HABBAL, AND M. ORTIZ. **Optimal Transportation Meshfree Approximation Schemes for Fluid and Plastic Flows.** *International Journal for Numerical Methods in Engineering*, **83**(12):1541–1579, 2010. 25
- [85] A. ORTIZ, M. A. PUSO, AND N. SUKUMAR. **Maximum-entropy meshfree method for compressible and near-incompressible elasticity.** *Computer Methods in Applied Mechanics and Engineering*, **199**(25–28):1859–1871, 2010. 25
- [86] A. ORTIZ, M. A. PUSO, AND N. SUKUMAR. **Maximum-entropy meshfree method for incompressible media problems.** *Finite Elements in Analysis and Design*, **47**(6):572–585, 2011. 25

REFERENCES

- [87] C. T. WU AND W. HU. **Meshfree-enriched simplex elements with strain smoothing for the finite element analysis of compressible and nearly incompressible solids.** *Computer Methods in Applied Mechanics and Engineering*, **200**(45–46):2991–3010, 2012. 25
- [88] W. HU, C. T. WU, AND M. KOISHI. **A displacement-based nonlinear finite element formulation using meshfree-enriched triangular elements for two-dimensional large deformation analysis of elastomers.** *Finite Elements in Analysis and Design*, **50**(1):161–172, 2012. 25
- [89] A. ROSOLEN, D. MILLÁN, AND M. ARROYO. **On the optimum support size in meshfree methods: a variational adaptivity approach with maximum entropy approximants.** *International Journal for Numerical Methods in Engineering*, **82**(7):868–895, 2010. 25
- [90] D. MILLÁN, A. ROSOLEN, AND M. ARROYO. **Thin shell analysis from scattered points with maximum-entropy approximants.** *International Journal for Numerical Methods in Engineering*, **85**(6):723–751, 2011. 25, 51
- [91] D. MILLÁN, A. ROSOLEN, AND M. ARROYO. **Nonlinear manifold learning for meshfree finite deformation thin shell analysis.** *International Journal for Numerical Methods in Engineering*, **93**:685–713, 2013. 25
- [92] J. S. HALE AND P. M. BAIZ. **A locking-free meshfree method for the simulation of shear-deformable plates based on a mixed variational formulation.** *Computer Methods in Applied Mechanics and Engineering*, 2012. <http://dx.doi.org/10.1016/j.cma.2012.06.010>. 25
- [93] L. L. YAW, N. SUKUMAR, AND S. K. KUNNATH. **Meshfree co-rotational formulation for two-dimensional continua.** *International Journal for Numerical Methods in Engineering*, **79**(8):979–1003, 2009. 25, 29
- [94] G. QUARANTA, S. K. KUNNATH, AND N. SUKUMAR. **Maximum-entropy meshfree method for nonlinear static analysis of planar reinforced concrete structures.** *Engineering Structures*, **42**:179–189, 2012. 25
- [95] C. J. CYRON, K. NISSEN, V. GRAVEMEIER, AND W. A. WALL. **Stable meshfree methods in fluid mechanics based on Green’s functions.** *Computational Mechanics*, **46**(2):287–300, 2010. 25
- [96] C. J. CYRON, K. NISSEN, V. GRAVEMEIER, AND W. A. WALL. **Information-flux maximum-entropy approximation schemes for convection-diffusion problems.** *International Journal for Numerical Methods in Fluids*, **64**(10–12):1180–1200, 2010. 25
- [97] K. NISSEN, C. J. CYRON, V. GRAVEMEIER, AND W. A. WALL. **Information-flux method: a meshfree maximum-entropy Petrov-Galerkin method including stabilised finite element methods.** *Computer Methods in Applied Mechanics and Engineering*, 2012. <http://dx.doi.org/10.1016/j.cma.2012.05.015>. 25
- [98] A. ROSOLEN, C. PECO, AND M. ARROYO. **An adaptive meshfree method for phase-field models of biomembranes. Part I: Approximation with maximum-entropy basis functions.** *Journal of Computational Physics*, **249**(0):303 – 319, 2013. 25
- [99] C. PECO, A. ROSOLEN, AND M. ARROYO. **An adaptive meshfree method for phase-field models of biomembranes. Part II: A Lagrangian approach for membranes in viscous fluids.** *Journal of Computational Physics*, **249**(0):320 – 336, 2013. 25
- [100] F. FRATERNALI, C. D. LORENZ, AND G. MARCELLI. **On the estimation of the curvatures and bending rigidity of membrane networks via a local maximum-entropy approach.** *Journal of Computational Physics*, **231**(2):528–540, 2012. 25, 29
- [101] P. SURYANARAYANA, K. BHATTACHARYA, AND M. ORTIZ. **A mesh-free convex approximation scheme for Kohn-Sham density functional theory.** *Journal of Computational Physics*, **230**(13):5226–5238, 2011. 25
- [102] C. E. SHANNON. **A Mathematical Theory of Communication.** *The Bell Systems Technical Journal*, **27**:379–423, 1948. 26
- [103] E.T. JAYNES. **Information theory and statistical mechanics.** *Physics Reviews*, **106**:620–630, 1957. 26
- [104] V.T. RAJAN. **Optimality of the Delaunay triangulation in R^d .** *Discrete and Computational Geometry*, **12**(2):189–202, 1994. 27
- [105] J. E. SHORE AND R. W. JOHNSON. **Axiomatic Derivation of the Principle of Maximum Entropy and the Principle of Minimum Cross-Entropy.** *IEEE Transactions on Information Theory*, **26**(1):26–36, 1980. 27
- [106] N. SUKUMAR. *Fortran 90 Library for Maximum-Entropy Basis Functions.* User’s Reference Manual Version 1.4. Code available at <http://www.imechanica.org/node/3424>, 2008. 29

REFERENCES

- [107] F. GRECO AND N. SUKUMAR. **Derivatives of maximum-entropy basis functions on the boundary: Theory and computations.** *International Journal for Numerical Methods in Engineering*, **94**(12):1123–1149, 2013. 31, 51
- [108] T.J.R. HUGHES, J.A. COTTRELL, AND Y. BAZILEVS. **Isogeometric analysis: CAD, finite elements, NURBS, exact geometry and mesh refinement.** *Computer Methods in Applied Mechanics and Engineering*, **194**:4135–4195, 2005. 32, 34
- [109] J.A. COTTRELL, T.J.R. HUGHES, AND Y. BAZILEVS. *Isogeometric Analysis: Toward Integration of CAD and FEA.* John Wiley & Sons, Ltd., 2009. 32
- [110] Y. BAZILEVS, V.M. CALO, J.A. COTTRELL, J.A. EVANS, T.J.R. HUGHES, S. LIPTON, M.A. SCOTT, AND T.W. SEDERBERG. **Isogeometric analysis using T-Splines.** *Computer Methods in Applied Mechanics and Engineering*, **199**(5–8):229–263, 2010. 32
- [111] L. BEIRÃO DA VEIGA, A. BUFFA, D. CHO, AND G. SANGALLI. **IsoGeometric analysis using T-splines on two-patch geometries.** *Computer Methods in Applied Mechanics and Engineering*, **200**(21–22):1787–1803, 2011. 32
- [112] M.R. DÖRFEL, B. JÜTTLER, AND B. SIMEON. **Adaptive isogeometric analysis by local h-refinement with T-Splines.** *Computer Methods in Applied Mechanics and Engineering*, **199**(5–8):264–275, 2010. 32
- [113] N. NGUYEN-THANH, H. NGUYEN-XUAN, S.P.A. BORDAS, AND T. RABCUK. **Isogeometric analysis using polynomial splines over hierarchical T-meshes for two-dimensional elastic solids.** *Computer Methods in Applied Mechanics and Engineering*, **200**(21–22):1892–1908, 2011. 32
- [114] M.A. SCOTT, X. LI, T.W. SEDERBERG, AND T.J.R. HUGHES. **Local refinement of analysis-suitable T-splines.** *Computer Methods in Applied Mechanics and Engineering*, **213–216**:206–222, 2012. 32
- [115] A.-V. VUONG, C. GIANNELLI, B. JÜTTLER, AND B. SIMEON. **A hierarchical approach to adaptive local refinement in isogeometric analysis.** *Computer Methods in Applied Mechanics and Engineering*, **200**(49–52):3554–3567, 2011. 32
- [116] H.-J. KIM, Y.-D. SEO, AND S.-K. YOUN. **Isogeometric analysis with trimming technique for problems of arbitrary complex topology.** *Computer Methods in Applied Mechanics and Engineering*, **199**(45–48):2796–2812, 2010. 32
- [117] D. A. DUNAVANT. **High degree efficient symmetrical Gaussian quadrature rules for the triangle.** *International Journal for Numerical Methods in Engineering*, **21**(6):1129–1148, 1985. 39
- [118] P. WRIGGERS. **Computational Contact Mechanics.** *Computational Mechanics*, **32**:141–141, 2003. 40, 52, 53
- [119] M.E. MATZEN, T. CICHOSZ, AND M. BISCHOFF. **A point to segment contact formulation for isogeometric, NURBS based finite elements.** *Computer Methods in Applied Mechanics and Engineering*, **255**(0):27 – 39, 2013. 41, 42
- [120] PER OLOF PERSSON AND GILBERT STRANG. **A Simple Mesh Generator in MATLAB.** *SIAM Review*, **46**:2004, 2004. 47
- [121] F. BREZZI. **On the existence, uniqueness and approximation of saddle-point problems arising from lagrangian multipliers.** *ESAIM: Mathematical Modelling and Numerical Analysis - Modlisation Mathématique et Analyse Numrique*, **8**(R2):129–151, 1974. 49
- [122] IVO BABUKA. **The finite element method with Lagrangian multipliers.** *Numerische Mathematik*, **20**(3):179–192, 1973. 49
- [123] RAMON CODINA. **Comparison of some finite element methods for solving the diffusion-convection-reaction equation.** *Computer Methods in Applied Mechanics and Engineering*, **156**(14):185 – 210, 1998. 49, 52
- [124] TERI BARTH, PAVEL BOCHEV, MAX GUNZBURGER, AND JOHN SHADID. **A Taxonomy of Consistently Stabilized Finite Element Methods for the Stokes Problem.** *SIAM J. Sci. Comput.*, **25**(5):1585–1607, May 2004. 49, 51
- [125] PAVEL BOCHEV AND MAX GUNZBURGER. **An Absolutely Stable Pressure-Poisson Stabilized Finite Element Method for the Stokes Equations.** *SIAM J. Numer. Anal.*, **42**(3):1189–1207, March 2004. 49, 51, 52
- [126] F. BREZZI AND J. PITKARANTA. *On the stabilization of finite element approximations of the Stokes equations*, **10** of *Notes on Numerical Fluid Mechanics*, chapter Efficient Solutions of Elliptic Systems, pages 11–19. Viewig, Braunschweig, 1984. 50, 51
- [127] THOMAS J.R. HUGHES, LEOPOLDO P. FRANCA, AND MARC BALESTRA. **A new finite element formulation for**

REFERENCES

- computational fluid dynamics: V. Circumventing the babuka-brezzi condition: a stable Petrov-Galerkin formulation of the stokes problem accommodating equal-order interpolations.** *Computer Methods in Applied Mechanics and Engineering*, **59**(1):85 – 99, 1986. 51
- [128] K.E. JANSEN, S.S. COLLIS, C. WHITING, AND F. SHAKIB. **A better consistency for low-order stabilized finite element methods.** *Computer Methods in Applied Mechanics and Engineering*, **174**(1-2):153–170, 1999. cited By (since 1996)58. 52
- [129] ISAAC HARARI AND THOMAS J.R. HUGHES. **What are C and h?: Inequalities for the analysis and design of finite element methods.** *Computer Methods in Applied Mechanics and Engineering*, **97**(2):157 – 192, 1992. 52

Dichiarazione

La presente tesi è cofinanziata con il sostegno della Commissione Europea, Fondo Sociale Europeo e della Regione Calabria. L'autore è il solo responsabile di questa tesi e la Commissione Europea e la Regione Calabria declinano ogni responsabilità sull'uso che potrà essere fatto delle informazioni in essa contenute

Arcavacata, 30 Novembre 2013